The Astrophysical Journal, 665:492–511, 2007 August 10

c2d *SPITZER* IRS SPECTRA OF DISKS AROUND T TAURI STARS. III. [Ne II], [Fe I], AND H_2 GAS-PHASE LINES

Fred Lahuis,[1,2] Ewine F. van Dishoeck,[1] Geoffrey A. Blake,[3] Neal J. Evans, II,[4] Jacqueline E. Kessler-Silacci,[4] and Klaus M. Pontoppidan[3]

Received 2007 March 6; accepted 2007 April 15

ABSTRACT

We present a survey of mid-infrared gas-phase lines toward a sample of 76 circumstellar disks around low-mass pre–main-sequence stars from the *Spitzer* "Cores to Disks" legacy program. We report the first detections of [Ne II] and [Fe I] toward classical T Tauri stars in ~20% and ~9% of our sources, respectively. The observed [Ne II] line fluxes and upper limits are consistent with [Ne II] excitation in an X-ray irradiated disk around stars with X-ray luminosities $L_X = 10^{29}$–10^{31} erg s^{-1}. [Fe I] is detected at $\sim 10^{-5}$ to $10^{-4}\,L_\odot$, but no [S I] or [Fe II] is detected down to $\sim 10^{-6}\,L_\odot$. The [Fe I] detections indicate the presence of gas-rich disks with masses of $\gtrsim 0.1\,M_J$. No H_2 0–0 $S(0)$ and $S(1)$ disk emission is detected, except for $S(1)$ toward one source. These data give upper limits on the warm ($T \sim$ 100–200 K) gas mass of a few Jovian masses, consistent with recent T Tauri disk models that include gas heating by stellar radiation. Compact disk emission of hot ($T \gtrsim 500$ K) gas is observed through the H_2 0–0 $S(2)$ and/or $S(3)$ lines toward ~8% of our sources. The line fluxes are, however, higher by more than an order of magnitude than those predicted by recent disk models, even when X-ray and excess UV radiation are included. The [Ne II]/H_2 0–0 $S(2)$ ratios for these sources are similarly lower than predicted, consistent with the presence of an additional hot molecular gas component not included in current disk models. Oblique shocks of stellar winds interacting with the disk can explain many aspects of the hot gas emission but are inconsistent with the nondetection of [S I] and [Fe II] lines.

Subject headings: circumstellar matter — infrared: ISM — planetary systems: protoplanetary disks — stars: evolution — stars: low-mass, brown dwarfs — surveys

1. INTRODUCTION

Circumstellar disks are a natural and important phenomenon in low-mass star formation. The ability to trace the evolution of the disk dust and gas content is crucial to understanding their chemistry and physics and the formation of planets. Observed disks reveal a large source-to-source variation and suggest a complex evolution from young gas-rich disks to tenuous debris disks. Disk geometries are observed to range from almost flat to strongly flaring disks (Dullemond & Dominik 2004), and disks with large inner cavities are found (Calvet et al. 2002; Bouwman et al. 2003; Forrest et al. 2004; Brown et al. 2007). Observations of silicates and spectral energy distributions (SEDs) present evidence for grain growth and settling of large grains to the disk midplane (van Boekel et al. 2003; D'Alessio et al. 2006; Kessler-Silacci et al. 2006). Different degrees of grain heating and radial mixing in the disks (van Boekel et al. 2005) and varying PAH abundances affect the heating of the upper layers of the disk (Habart et al. 2006; Geers et al. 2006). Most of these disk properties are derived from infrared solid-state features and from near-infrared to millimeter continuum observations and associated SED modeling. However, such data give little information about the gas in the disk.

Gas plays an important role in the structure and evolution of disks, influencing the temperature and density gradients, chemistry, dust dynamics, and eventually the formation of gas-rich and gas-poor planets (Gorti & Hollenbach 2004). Observational diagnostics of the physical conditions of the gas, in particular its mass and temperature, are therefore highly relevant to studies of disk evolution and planet formation. Central questions are how the gas in the disk is dissipated, what drives the disk heating and gas clearing, and what the associated timescales are. The small number of observed transitional objects between the classical T Tauri phase (large Hα equivalent width, thought to be accreting) or the weak-line T Tauri phase (small Hα, nonaccreting), both with massive optically thick disks, and the more evolved phase, with optically thin or no disks, suggests that disk clearing timescales are short (few $\times 10^5$ yr) compared to the disk lifetime of a few Myr (L. A. Cieza et al. 2007; Haisch et al. 2001). In addition, combined near-IR, mid-IR, and millimeter observations imply that the disk clearing happens nearly simultaneously across the disk (see, e.g., Kenyon & Hartmann 1995; Hartmann et al. 2005; Takeuchi et al. 2005). Alexander et al. (2006) present a new evolutionary model combining viscous evolution with photoevaporation of the disk to address these issues. In this mechanism, the disk is cleared through an evaporative flow originating from the disk surface layers as a result of UV and/or X-ray heating (see, e.g., Hollenbach et al. 2000; Clarke et al. 2001; Kamp & Dullemond 2004; Dullemond et al. 2007). Information about the temperature and mass of the warm gas and constraints on the details of the heating processes across the disk are therefore vital for advancing the current models.

Models of gas heating include UV and X-ray radiation from the star itself as well as possible excess radiation due to accretion (e.g., Jonkheid et al. 2004, 2007; Gorti & Hollenbach 2004; Kamp & Dullemond 2004; Nomura & Millar 2005). The resulting gas temperatures in the surface layers out to large radii are significantly higher than those of the dust as a result of the photoelectric effect on small grains and PAHs. Gas temperatures may reach values of up to a few thousand kelvins. Once grains have

[1] Leiden Observatory, Leiden University, P.O. Box 9513, 2300 RA Leiden, Netherlands.
[2] SRON Netherlands Institute for Space Research, P.O. Box 800, 9700 AV Groningen, Netherlands.
[3] Division of Geological and Planetary Sciences 150-21, California Institute of Technology, Pasadena, CA 91125.
[4] Department of Astronomy, University of Texas at Austin, 1 University Station C1400, Austin, TX 78712-0259.

grown to micron sizes or larger, however, the gas temperature is significantly decreased unless PAHs are still present (Jonkheid et al. 2004, 2006, 2007). Nomura & Millar (2005) explicitly include the excitation of H_2 by UV and collisions for a disk around a T Tauri star with and without excess UV and make predictions for line intensities that can be tested against observations. Glassgold et al. (2007) have studied the case of X-ray heating and have shown that the ionized neon fine-structure line emission may provide unique tracers of X-ray heating in the disk surface since neon cannot be photoionized by radiation with energies below 13.6 eV.

Observational studies of the gas and its temperature have mostly focused on the hot inner and the cold outer regions of disks. High-resolution CO $v = 1$–0 vibration-rotation lines at 4.7 μm (Najita et al. 2003; Brittain et al. 2003; Blake & Boogert 2004) and H_2 2.1 μm 1–0 $S(1)$ (Bary et al. 2003) show gas with temperatures $\sim$1000–3000 K in the surface layers out to $\sim$1 AU. H_2O emission from SVS 13 (Carr et al. 2004) and molecular absorption of C_2H_2, HCN, and CO_2 in the disk of IRS 46 (Lahuis et al. 2006a) also indicate hot temperatures in the inner few AU of several hundred kelvins. In contrast, millimeter CO surveys probe the cold gas throughout the outer disk, where the dust is optically thin (e.g., Koerner & Sargent 1995; Duvert et al. 2000; Thi et al. 2001; Dutrey et al. 2003; Dent et al. 2005). Its use as a gas mass tracer, however, is limited as a result of both strong photodissociation at low extinction and freezeout in the disk interior. Gas temperature determinations range from $<$20 K near the midplane (Dartois et al. 2003; Piétu et al. 2007) to 40 K or higher in the intermediate and surface layers (van Zadelhoff et al. 2001; Qi et al. 2006).

The mid-IR H_2 and atomic fine-structure lines are best suited as direct tracers of the warm ($\sim$100 K) gas in the intermediate zones of disks at radii of a few AU out to several tens of AU, i.e., the planet-forming zones of disks. The *Infrared Space Observatory* (*ISO*) provided the first opportunity to probe this warm gas in disks around Herbig Ae and T Tauri stars. Thi et al. (2001) suggested that large amounts ($\sim$0.01–100 M_J) of gas could reside in disks around young T Tauri stars, but this has not been confirmed by subsequent ground-based observations (Richter et al. 2002; Sheret et al. 2003; Sako et al. 2005).

The sensitive Infrared Spectrograph (IRS; Houck et al. 2004) on board the *Spitzer Space Telescope* (Werner et al. 2004) brings the detection of these lines within reach for young solar-mass stars in nearby star-forming regions. The combination of high sensitivity, moderate spectral resolution $R = \lambda/\Delta\lambda = 600$, and modest spatial resolution makes *Spitzer* well suited for the direct study of the gas in and around low-mass young stars in nearby ($\lesssim$300 pc) clouds through the mid-IR lines of various species.

We present here an overview of gas-phase lines detected in disks observed in the *Spitzer* legacy program "From Molecular Cores to Planet Forming Disks" ("Cores to Disks" or c2d; Evans et al. 2003), which has collected a large sample of IRS spectra toward sources in the nearby Chamaeleon, Lupus, Perseus, Ophiuchus, and Serpens star-forming regions. High signal-to-noise ratio 5–38 μm spectra have been obtained for 226 sources at all phases of star and planet formation up to ages of $\sim$5 Myr. From this sample, 76 disk sources, identified by showing either the 10 or 20 μm silicate bands in emission, have been selected. In §§ 2 and 3 the source selection and data reduction are explained. In § 4 the observed atomic fine-structure and H_2 emission lines and the derived parameters are presented. In § 5 the results are reviewed in the context of currently available disk models. This paper forms a complement to the searches for the mid-infrared lines of H_2 and other species toward more evolved disks studied in other *Spitzer* programs (e.g., Hollenbach et al. 2005; Pascucci et al. 2006, 2007).

2. OBSERVATIONS

The data presented in this study were selected from the sample of IRS spectra observed within the *Spitzer* c2d legacy program. The c2d IRS program consists of two programs of comparable size, referred to as the first- and second-look programs. The first-look program (PID 172) was restricted primarily to known low-mass young stars, embedded young stellar objects (YSOs) and pre–main-sequence stars with disks of mass $M < 2\ M_\odot$ and age $\lesssim$5 Myr, and a sample of background stars. A few Herbig Ae stars are included as well. The c2d source selection criteria were defined to be complementary to those of the *Spitzer* legacy program "The Formation and Evolution of Planetary Systems" (FEPS; Meyer et al. 2006). The second-look program (PID 179) was, for the most part, devoted to IRS follow-up spectroscopy of sources discovered in the IRAC and MIPS mapping surveys, including a newly discovered cluster of young stars in Serpens (Harvey et al. 2006). For all first-look observations, the integration times for the short-high (SH) and long-high (LH) modules ($R = 600$, 10–37 μm) were chosen such that theoretical signal-to-noise ratios (S/Ns) of at least 100 and 50 on the continuum were obtained for sources brighter and fainter than 500 mJy, respectively. Deeper integrations were not feasible within the c2d program. Spectra taken using the short-low (SL) or long-low (LL) modules ($R = 60$–120, 5–14 and 14–38 μm, respectively) always reach theoretical S/Ns greater than 100. For the second-look IRS targets similar S/N limits were obtained wherever possible. However, since the second-look contained a number of very weak sources (down to a few millijanskys) this was not always achieved.

2.1. *Source Selection*

The sources presented in this paper were all selected to show either of the 10 or 20 μm silicate bands in emission. A total of 76 sources were chosen; see Kessler-Silacci et al. (2006) for the 47 first-look disk sources with silicate emission. This selection excludes most edge-on disk sources ($i \gtrsim 65^\circ$) such as CRBR 2422.8-3423 (Pontoppidan et al. 2005), IRS 46 (Lahuis et al. 2006a), and the "Flying Saucer" (Pontoppidan et al. 2007), with the exception of the high-inclination sources EC 82 (Pontoppidan & Dullemond 2005) and VV Ser, which are included in this paper. Gas-phase lines toward edge-on disk sources will be discussed in a separate paper together with the embedded Class 0 and I sources (F. Lahuis et al. 2007, in preparation). The selected sources are listed in Table 1, which gives the basic observing and source parameters, e.g., the adopted distances.

2.2. *Short-High Minimaps*

In an early phase of the c2d project molecular hydrogen and [Ne II] lines were detected toward some of the c2d sources. As part of the second-look program, follow-up minimaps were taken using the SH module to check for extended emission at offset positions of $\sim$10″–15″ with respect to the sources. Five maps were defined to include off-source observations around eight sources. Three of these are disk sources included in our sample, Sz 102 (Krautter's star), Haro 1–17, and EC 74. Figure 1 shows the observed H_2 0–0 $S(1)$, $S(2)$, and [Ne II] emission from the first-look on-source observations together with the off-source observations from the second-look minimaps. The maps show

TABLE 1
SOURCE LIST

No. (1)	Source (2)	R.A. (3)	Decl. (4)	AOR (5)	Tint (SL, SH, LH)[a] (s) (6)	Class (7)	D[b] (pc) (8)	Age (Myr) (9)	Spectral Type (10)	References (11)
1.....	RNO 15	3 27 47.7	30 12 04.3	5633280	(14 × 1, 31 × 2, 60 × 1) × 2	TTs	250	...	...	1, 2
2.....	Lk Hα 270	3 29 17.7	31 22 45.1	5634048	(14 × 2, 31 × 2, 60 × 2) × 2	TTs	250	0.01	K2.5–K7	3
3.....	Lk Hα 271	3 29 21.9	31 15 36.4	11827968	(14 × 2, 121 × 2, 60 × 2) × 2	TTs	250	...	K3–K5	3
4.....	Lk Hα 326	3 30 44.0	30 32 46.7	5634304	(14 × 2, 31 × 4, 60 × 1) × 2	TTs	250	0.3	G–M0	3, 4, 5
5.....	Lk Hα 327	3 33 30.4	31 10 50.5	5634560	(14 × 1, 6 × 2, 14 × 2) × 2	TTs	250	0.7–1.4	A9–K2	2, 3
6.....	Lk Hα 330	3 45 48.3	32 24 11.9	5634816	(14 × 1, 31 × 1, 60 × 1) × 2	CTTs	250	5.7	G3	2, 3
7.....	IRAS 03446+3254	3 47 47.1	33 04 03.4	5635072	(14 × 1, 121 × 2, 60 × 1) × 2	TTs	250	...	...	1, 2, 6, 7
8.....	Lk Ca 8	4 24 57.1	27 11 56.4	9832960	(–, 31 × 8, 60 × 2) × 2	CTTs	140	...	M0	8, 9
9.....	IQ Tau	4 29 51.6	26 06 45.0	9832704	(–, 31 × 2, 60 × 2) × 2	WTTs	140	1.2	M0–M0.5	3, 8
10.....	FX Tau	4 30 29.6	24 26 45.2	9832448	(–, 31 × 2, 60 × 2) × 2	C+WTTs	140	...	M1–M4	10
11.....	V710 Tau	4 31 57.8	18 21 36.4	5636608	(–, 121 × 2, 60 × 4) × 2	C+WTTs	140	...	M0.5–M3	8
12.....	DN Tau	4 35 27.4	24 14 58.9	9831936	(–, 31 × 4, 60 × 2) × 2	CTTs	140	...	M0	10
13.....	CoKu Tau 3	4 35 40.9	24 11 08.5	9831936	(–, 31 × 4, 60 × 2) × 2	CTTs	140	...	M1	10
14.....	CoKu Tau 4	4 41 16.8	28 40 00.5	5637888	(–, 31 × 2, 60 × 4) × 2	CTTs	140	1.2–1.6	M1.5	2, 8, 11
15.....	BF Ori	5 37 13.3	−6 35 00.6	5638144	(14 × 1, 31 × 1, 60 × 1) × 2	HAeBe	400	2.0	A5–F6	2
16.....	RR Tau	5 39 30.5	26 22 27.1	5638400	(14 × 1, 31 × 1, 60 × 1) × 2	HAeBe	160	0.6	B8–A5	2
17.....	IRAS 08267−3336	8 28 40.7	−33 46 22.4	5639168	(14 × 1, 31 × 2, 60 × 1) × 2	TTs	400?	2.0	K2–K3	2, 3
18.....	SX Cha	10 55 59.7	−77 24 40.0	5639424	(–, 121 × 1, 60 × 2) × 2	TTs	178	1.0–4.0	M0.5	2, 12, 13, 14
19.....	SY Cha	10 56 30.5	−77 11 39.5	5639424	(–, 121 × 1, 60 × 2) × 2	TTs	178	1.4–5.0	M0	2, 12, 13, 15, 16
20.....	TW Cha	10 59 01.1	−77 22 40.8	5639680	(–, 121 × 2, 60 × 2) × 2	TTs	178	16.8–20.0	K0–M0	2, 12, 13, 14, 15, 16, 17
21.....	Ced 110 IRS 6	11 07 09.2	−77 23 04.2	5639680	(–, 121 × 2, 60 × 2) × 2	1	178	...	...	17, 18, 19
22.....	B35	11 07 21.5	−77 22 11.7	5639680	(–, 121 × 2, 60 × 2) × 2	TTs	178	0.1	M2	17, 18, 19
23.....	VW Cha	11 08 01.5	−77 42 28.8	5639680	(–, 121 × 2, 60 × 2) × 2	CTTs	178	0.2–2.4	K2–K7	2, 3, 12, 13, 14, 15, 17, 19, 20
24.....	VZ Cha	11 09 23.8	−76 23 20.8	5640448	(–, 121 × 2, 60 × 2) × 2	TTs	178	4.0–10.0	K6–K7	2, 3, 12, 13, 14, 15, 17, 20
25.....	WX Cha	11 09 58.8	−77 37 08.8	5640192	(–, 121 × 1, 60 × 2) × 2	TTs	178	0.8–5.0	K7–M0	2, 3, 12, 13, 14, 15, 17, 19
26.....	ISO-ChaI 237	11 10 11.4	−76 35 29.0	5640448	(–, 121 × 2, 60 × 2) × 2	TTs	178	...	M0	2, 17, 19
27.....	C7-11	11 10 38.0	−77 32 39.9	5640192	(–, 121 × 1, 60 × 2) × 2	TTs	178	0.2–1.0	K3	2, 12, 15, 17, 19
28.....	HM 27	11 10 49.6	−77 17 51.7	5640192	(–, 121 × 1, 60 × 2) × 2	TTs	178	2.4–40.0	K7	2, 3, 12, 13, 15, 17, 19
29.....	XX Cha	11 11 39.7	−76 20 15.0	5640448	(–, 121 × 2, 60 × 2) × 2	TTs	178	1.9–40.0	M1–M2	2, 12, 13, 14, 15, 17
30.....	HD 98922	11 22 31.7	−53 22 11.3	5640704	(–, 6 × 1, 14 × 1) × 2	HAeBe	>540	...	B9	2
31.....	HD 101412	11 39 44.5	−60 10 27.8	5640960	(14 × 1, 31 × 1, 60 × 1) × 2	HAeBe	160	...	B9.5	2
32.....	T Cha	11 57 13.5	−79 21 31.3	5641216	(–, 31 × 2, 60 × 1) × 2	TTs	66	4.1–12.5	G2–K0	2, 3, 12, 13, 15
33.....	IRAS 12535−7623	12 57 11.8	−76 40 11.6	11827456	(–, 121 × 1, 60 × 2) × 2	TTs	178	0.2	M0	2, 13, 15
34.....	Sz 50	13 00 55.4	−77 10 22.1	11827456	(–, 121 × 1, 60 × 2) × 2	TTs	178	1.7	K7–M3	2, 13, 15
35.....	ISO-ChaII 54	13 00 59.2	−77 14 02.8	15735040	(14 × 2, 31 × 4, –) × 2	BD	178	...	...	21
36.....	DL Cha	13 06 08.4	−77 06 27.4	5642240	(–, 6 × 2, 6 × 5) × 2	TTs	178	...	M6	2, 13, 15, 22
37.....	HD 132947	15 04 56.0	−63 07 52.7	5643008	(14 × 1, 31 × 2, 241 × 2) × 2	HAeBe	>60	...	A0	2, 13, 15, 22
38.....	HD 135344	15 15 48.4	−37 09 15.8	5657088	(–, 121 × 1, 60 × 2) × 2	HAeBe	140	17.0	A0–F4	2
39.....	HT Lup	15 45 12.9	−34 17 30.5	5643264	(14 × 1, 31 × 1, 60 × 1) × 2	TTs	145	0.4–2.3	K2	2, 3, 14, 23, 24
40.....	HT Lup	15 45 12.9	−34 17 30.5	9829120	(14 × 2, 31 × 2, 60 × 2) × 1	TTs	145	0.4–2.3	K2	2, 3, 14, 23, 24
41.....	GW Lup	15 46 44.7	−34 30 35.3	5643520	(14 × 1, 121 × 2, 60 × 4) × 2	TTs	100	1.3–3.4	M2–M4	2, 3, 24
42.....	Sz 73	15 47 57.0	−35 14 35.2	5644032	(14 × 1, 31 × 1, 60 × 1) × 2	TTs	100	2.6–5.4	K2–M	2, 3, 24
43.....	GQ Lup	15 49 12.1	−35 39 05.0	5644032	(14 × 1, 31 × 1, 60 × 1) × 2	TTs	100	0.1–1.0	K7–M0	2, 3, 14, 23, 24
44.....	IM Lup	15 56 09.2	−37 56 06.4	5644800	(14 × 1, 31 × 2, 60 × 1) × 2	TTs	140	0.1–1.5	M0	2, 3, 20, 24
45.....	RU Lup	15 56 42.3	−37 49 15.6	5644800	(14 × 1, 31 × 2, 60 × 1) × 2	CTTs	140	0.1–0.8	K3–M0	2, 23, 24
46.....	RY Lup	15 59 28.4	−40 21 51.1	5644544	(14 × 1, 31 × 1, 60 × 1) × 2	TTs	150	1.6–3.2	K0–K4	2, 3, 14, 24

TABLE 1—*Continued*

No. (1)	Source (2)	R.A. (3)	Decl. (4)	AOR (5)	Tint (SL, SH, LH)[a] (s) (6)	Class (7)	D[b] (pc) (8)	Age (Myr) (9)	Spectral Type (10)	References (11)
47	EX Lup	16 03 05.5	−40 18 24.8	5645056	(14 × 1, 31 × 1, 60 × 1) × 2	TTs	150	1.4–5.6	M0	2, 3, 14, 24
48	Sz 102	16 08 29.7	−39 03 11.2	9407488	(14 × 1, 121 × 2, 60 × 1) × 2	TTs	200	...	M0	2, 3, 24
49	AS 205	16 11 31.3	−18 38 26.2	5646080	(6 × 2, 6 × 2, 14 × 2) × 2	TTs	120	0.1–0.4	K5	2, 3, 20, 25
50	Haro 1–1	16 21 34.7	−26 12 27.0	9833472	(14 × 1, 31 × 4, 60 × 1) × 2	CTTs	125	13.1	K5–K7	3, 26, 27, 28
51	Haro 1–4	16 25 10.5	−23 19 14.5	9833216	(–, 31 × 2, 60 × 1) × 2	TTs	125	0.8	K4–K6	26
52	DoAr 24E	16 26 23.4	−24 21 00.0	5647616	(–, 31 × 1, 14 × 2) × 2	TTs	125	1.5–2.5	K0–K1	2, 20, 25, 29, 30, 31, 32
53	SR 21	16 27 10.3	−24 19 12.4	5647616	(–, 31 × 1, 14 × 2) × 2	TTs	125	1.0–3.0	F4–G2.5	2, 25, 30, 31, 33, 34, 35
54	IRS 51	16 27 39.8	−24 43 15.2	9829888	(–, 31 × 2, 14 × 2) × 2	2	125	0.8	G5–K7	3, 16, 25, 33
55	SR 9	16 27 40.3	−24 22 04.1	12027392	(–, 31 × 1, 60 × 2) × 2	TTs	125	0.8	K5–M2	2, 3, 25, 26, 29, 33, 34
56	V853 Oph	16 28 45.3	−24 28 18.8	12408576	(–, 31 × 4, 60 × 4) × 2	TTs	125	0.8	M1.5	25, 26
57	ROX 42C	16 31 15.7	−24 34 01.9	6369792	(–, 31 × 2, 60 × 1) × 2	TTs	125	3.7	K4–K6	16, 25
58	ROX 43A	16 31 20.1	−24 30 05.0	15914496	(–, 31 × 1, 60 × 2) × 2	TTs	125	12.2	G0	25, 34, 36
59	IRS 60	16 31 30.9	−24 24 39.6	6370048	(–, 31 × 1, 60 × 1) × 2	...	125	...	...	16, 25, 36, 37
60	Haro 1–16	16 31 33.5	−24 27 37.1	12664064	(–, 31 × 1, 60 × 1) × 2	TTs	125	0.5–1.9	K2–K3	14, 20, 25, 36
61	Haro 1–17	16 32 21.9	−24 42 14.8	11827712	(60 × 1, 121 × 4, 60 × 4) × 2	TTs	125	...	M2.5	2, 3, 25
62	RNO 90	16 34 09.2	−15 48 16.9	5650432	(14 × 1, 31 × 1, 14 × 2) × 2	TTs	140	6.0	G5	1, 2, 23, 25, 38, 39
63	Wa Oph 6	16 48 45.6	−14 16 35.8	5650688	(14 × 1, 31 × 1, 60 × 1) × 2	2	140	0.9	K7	25, 37
64	V1121 Oph	16 49 15.3	−14 22 08.8	5650688	(14 × 1, 31 × 1, 60 × 1) × 2	CTTs	125	0.5	K5	3, 23, 25, 37
65	HD 163296	17 56 21.3	−21 57 22.0	5650944	(–, 6 × 2, 14 × 2) × 2	HAeBe	122	4.0–6.0	A0–A2	2
66	HD 163296	17 56 21.3	−21 57 22.0	9830144	(–, 6 × 4, 14 × 4) × 1	HAeBe	122	4.0–6.0	A0–A2	2
67	VV Ser	18 28 47.9	0 08 39.8	5651200	(6 × 2, 31 × 1, 60 × 1) × 2	HAeBe	260	0.6	B1–A3	2
68	SSTc2d J182900.9+02931	18 29 00.9	0 29 31.6	13210112	(14 × 1, 31 × 2, –) × 2	...	260	...	...	...
69	SSTc2d J182909.8+03446	18 29 09.8	0 34 45.8	13210624	(14 × 1, 31 × 1, –) × 2	...	260	...	...	...
70	SSTc2d J182928.2+02257	18 29 28.2	−0 22 57.4	13210368	(14 × 1, 31 × 2, –) × 2	...	260	...	...	...
71	EC 74	18 29 55.7	1 14 31.6	9407232	(14 × 1, 121 × 1, 60 × 2) × 2	2	260	...	...	26
72	EC 82	18 29 56.9	1 14 46.7	9407232	(14 × 1, 121 × 1, 60 × 2) × 2	TTs	260	...	M0	2, 4, 26, 40
73	EC 90	18 29 57.7	1 14 06.0	9828352	(6 × 2, 31 × 1, 14 × 1) × 2	TTs	260	...	...	4, 26, 40, 41
74	EC 92	18 29 57.9	1 12 51.5	9407232	(14 × 1, 121 × 1, 60 × 2) × 2	TTs	260	...	K7–M2	18, 41, 42, 43
75	CK 4	18 29 58.2	1 15 21.6	9407232	(14 × 1, 121 × 1, 60 × 2) × 2	TTs	260	6.8	K3	2, 26, 40, 43, 44
76	Lk Hα 348	18 34 12.6	−0 26 21.8	9831424	(6 × 2, 6 × 2, 14 × 2) × 2	...	260	...	...	...

NOTES.—Units of right ascension are hours, minutes, and seconds, and units of declination are degrees, arcminutes, and arcseconds. The reference list given is not exhaustive.

[a] The integration time (ramp time × No. exposures) for the SL, SH, and LH modules and the number of dithers for each observation.

[b] Assumed cloud distances: Chamaeleon (178 pc; Whittet et al. 1997); Lupus I and IV (150 pc) and Lupus III (200 pc; S. Comeron 2007, in preparation); Ophiuchus (125 pc; de Geus et al. 1989); Perseus (250 pc; see discussion in Enoch et al. 2006); Taurus-Auriga (160 pc; Kenyon et al. 1994); Serpens (260 pc; Straizys et al. 1996), except for T Cha, HD 98922, and HD 163296 (van den Ancker et al. 1998); BF Ori (Parenago 1954); HD 101412 and HD 135344 (de Zeeuw et al. 1999); and HD 132947 (minimum Tycho distance).

REFERENCES.—(1) Clark 1991; (2) Kessler-Silacci et al. 2006; (3) Herbig & Bell 1988; (4) Casali & Eiroa 1996; (5) Ladd et al. 1993; (6) Beichman et al. 1984; (7) Myers et al. 1987; (8) Kenyon et al. 1998; (9) Edwards et al. 2006; (10) Beckwith et al. 1990; (11) Sargent et al. 2006; (12) Lawson et al. 1996; (13) Gauvin & Strom 1992; (14) Appenzeller et al. 1983; (15) Hartigan 1993; (16) Beichman et al. 1988; (17) Cambresy et al. 1998; (18) Pollanen & Feldman 1995; (19) Persi et al. 2000; (20) Schegerer et al. 2006; (21) Allers et al. 2006; (22) Lopez & Girard 1990; (23) Carballo et al. 1992; (24) Hughes et al. 1994; (25) Andre & Montmerle 1994; (26) Churchwell & Koornneef 1986; (27) Rydgren 1980; (28) Meyer et al. 1993; (29) Elias 1978; (30) Lada & Wilking 1984; (31) Ward-Thompson 1993; (32) Barsony et al. 1997; (33) Wilking et al. 1989; (34) Jensen & Mathieu 1997; (35) Brown et al. 2007; (36) Greene et al. 1994; (37) Ichikawa & Nishida 1989; (38) Reipurth et al. 1996; (39) Parker 1991; (40) Kaas 1999; (41) Haisch et al. 2002; (42) McMullin et al. 2000; (43) Hurt & Barsony 1996; (44) Zhang et al. 1988.

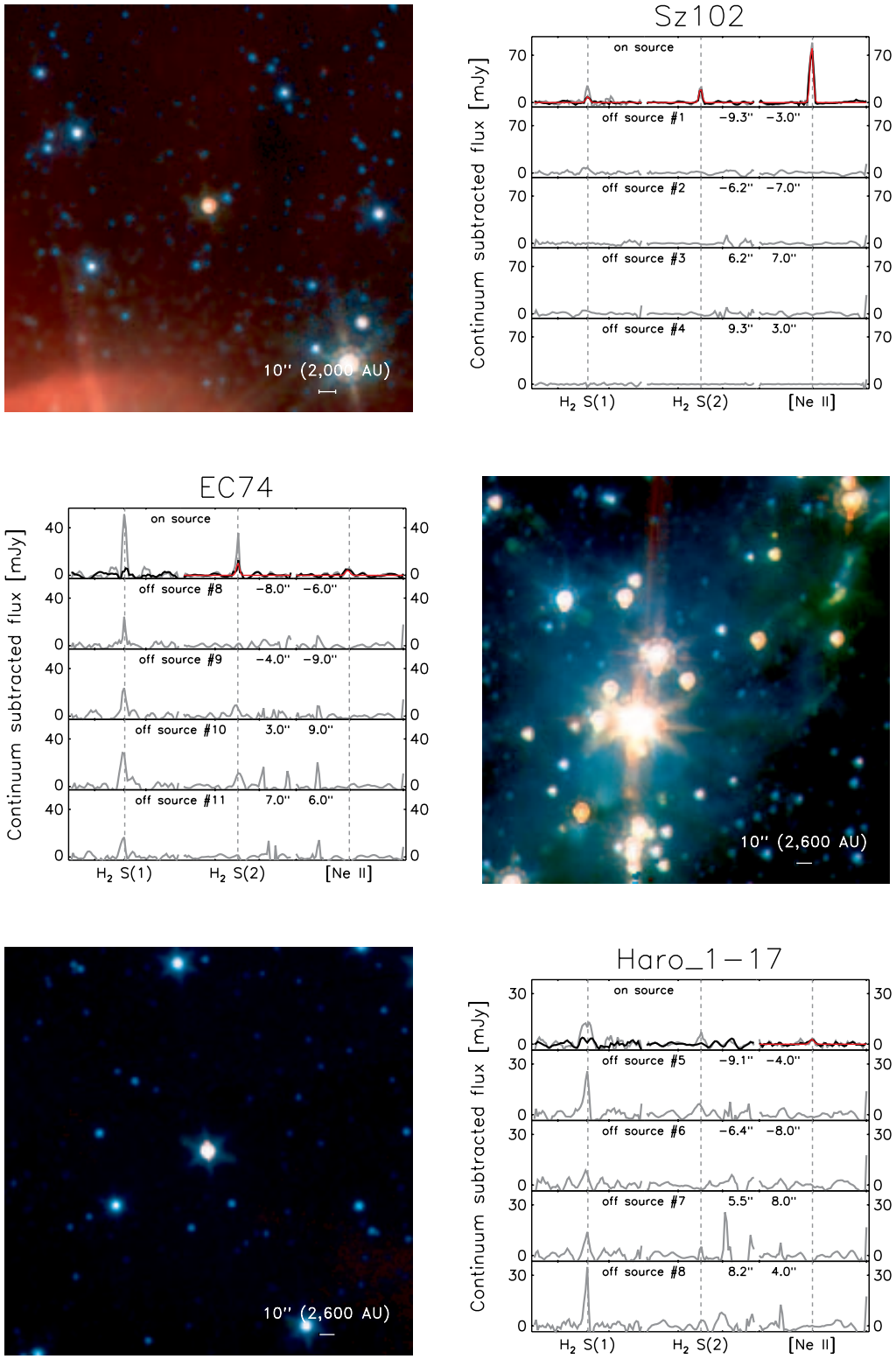

FIG. 1.—Observations of H_2 0–0 $S(1)$, $S(2)$, and [Ne II] emission observed on- and off-source toward Sz 102, EC 74, and Haro 1–17. The on-source observations were observed in the c2d first-look program, the follow-up off-source observations in the second-look program (see § 2). The images show *Spitzer* composites of IRAC1 (*blue*), IRAC2 (*green*), and IRAC4 (*red*) with the sources in the middle. The gray lines in the spectra show the total (compact source plus extended component) observed emission. The black lines show the source emission after correction for the extended component. The red lines show Gaussian fits to the compact source emission if observed at 3 σ or more. Although the S/N in the off-source positions is often poor, it illustrates the problem of extended and nonuniform H_2 emission. The [Ne II] is almost always limited to the source itself.

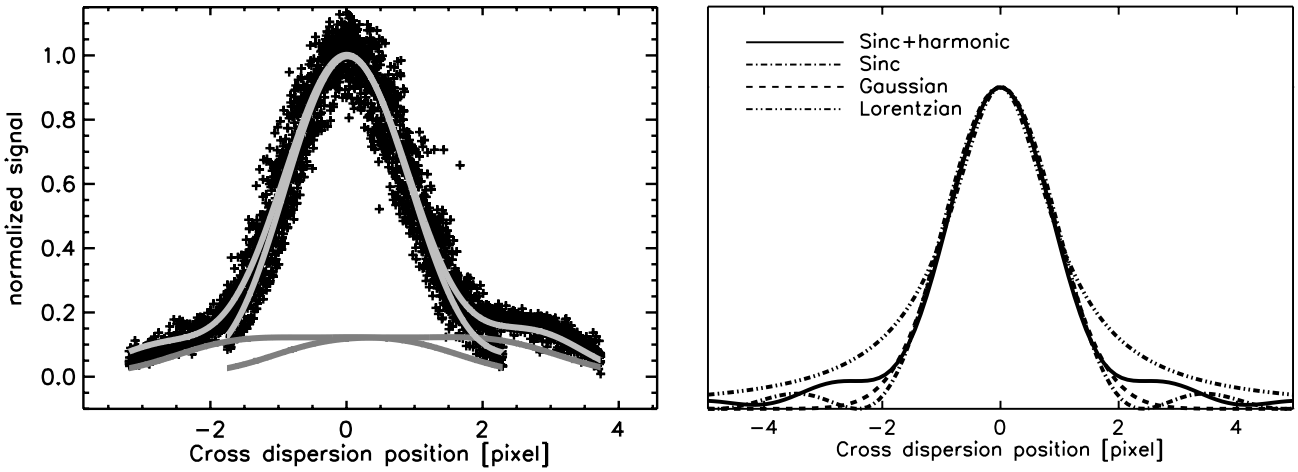

FIG. 2.—Illustration of the *Spitzer* IRS cross-dispersion profile used in the optimal extraction (see § 3.1). The left plot shows a fit to the IRS SH order 11 data of GW Lup, a source with a moderate but clear sky component in the IRS spectra. The rsc data (bcd data before flat-fielding) of both dither positions (*black plus signs*) are shown, normalized, collapsed along the dispersion direction, and corrected for the cross-dispersion dither offsets. Overplotted is the combined fit of the source profile plus the extended emission (*light gray lines*) and the extended emission (*dark gray lines*). The shape of the extended emission reflects the IRS flat field of the (for this source) assumed uniform extended emission. The right plot shows a comparison of an IRS PSF profile (sinc plus harmonics) compared to the profiles of an undistorted sinc, a Gaussian, and a Lorentzian profile with the same FWHM. Note the significant variation in the strength and shape of the profile wings. The correct characterization of both the width and the wings of the profile for all IRS orders is essential for extracting the proper source and sky spectra.

that most of the H_2 emission is extended, especially for the $S(1)$ line. However, fine-structure lines are usually seen to be limited to the source itself. Subsequent results using the c2d optimal extraction procedure (see § 3.1) confirm the conclusions drawn from the analysis of the minimaps.

The SH maps are not complete, since the time allocated for c2d spectroscopy did not allow us to observe fully sampled maps. The prime purpose of the maps is to confirm the presence or absence of extended emission. More extended mapping observations will be required to study the detailed spatial distribution and extent of the large-scale emission component.

3. DATA REDUCTION

The c2d reduction pipeline (Lahuis et al. 2006b) was used to reduce the IRS data, starting from the S13 and S14 archive data. The same c2d pipeline products as included in the final c2d legacy data delivery[5] were used for the spectral line analysis (see § 3.3). Most of the analysis focused on the SH and LH data, since the SL and LL data are generally limited by the low line/continuum ratio. The SL data were included and used to search for higher excitation H_2 0–0 lines, in particular the $S(3)$ transition.

3.1. *Separating Disk and Cloud Emission: Optimal Extraction*

A major concern when studying emission lines from YSOs is the possible contribution of extended (envelope or local cloud) emission in the sometimes complex star-forming regions. The spatial distribution of the emission, both in the continuum and in spectral lines, often prohibits the use of "sky" observations alone to correct for extended emission components. For this reason the c2d team has developed an optimal extraction algorithm for IRS pointed observations.

The *Spitzer* diffraction-limited beam is $\sim 4''$–$5''$ for the SH module (10–19.5 μm) and $\sim 7''$–$10''$ for the LH module (19–37 μm). At a distance of 100 pc this corresponds to physical sizes of $\sim$400–500 and $\sim$700–1000 AU, respectively. The clouds observed in the c2d program are located at distances ranging from 125 pc (Ophiuchus) to 260 pc (Serpens), increasing the physical area observed. The full IRS aperture in the SH and LH spatial direction is $\sim$2.5–3 times larger than the beam size. At the observed cloud distances this means that the aperture probes physical scales of several thousand AU. This makes it ideally suited for detecting cold or shocked H_2 emission from the extended (remnant) envelope, outflows, or the diffuse local cloud emission. For the disk sources studied in this work, however, the local cloud emission will potentially confuse the compact disk emission. Distinguishing between compact (disk) and extended (remnant envelope, outflow, or diffuse cloud) emission is therefore of vital importance for studying the emission lines originating in the circumstellar disks. The optimal point-spread function (PSF) extraction developed by the *Spitzer* c2d legacy team (Lahuis et al. 2006b) allows separation of the two components for all sources. The minimaps (see § 2.2) observed around selected sources confirm the results of the optimal extraction. See Figure 1 for an example of extended H_2 emission but compact [Ne II] emission. Other examples include Figures 3 and 4 in Geers et al. (2006) for separating extended cloud and compact disk PAH emission.

The optimal extraction uses an analytical cross-dispersion PSF for the source profile plus an extended emission component, to fit the observed cross talk or stray-light corrected echelle (SH and LH) and long-slit (SL and LL) images. The PSF is described by a sinc function with a harmonic distortion component, which results in a significant broadening of the profile wings (see Fig. 2). The wavelength dependence of the PSF parameters, the order trace, the width, and the harmonic distortion are characterized using a suite of high-S/N calibrator stars. For the extended emission component the flat-field cross-dispersion profile is used. The flux calibration is derived from the calibrator stars using Cohen templates and MARCS models (Decin et al. 2004) provided through the *Spitzer* Science Center. Lahuis et al. (2006b) give more details about the characterization and calibration of the c2d optimal extraction. The optimal extraction returns the total flux

[5] The c2d legacy data are accessible at http://ssc.spitzer.caltech.edu/legacy/c2dhistory.html.

TABLE 2

OBSERVED LINE FLUXES AND 1 σ UNCERTAINTIES

No. (1)	Source (2)	Distance (pc) (3)	H_2 $S(0)$ (4)	H_2 $S(1)$ (5)	H_2 $S(2)$ (6)	H_2 $S(3)$ (7)	[Ne II] (8)	[Ne III] (9)	[Fe I] (10)	[Fe II] 18 μm (11)	[Fe II] 25 μm (12)	[S I] (13)	[Si II] (14)
1.....	RNO 15	250	−(48)	−(63)	−(30)	−(470)	−(85)	−(69)	−(84)	−(78)	−(44)	−(43)	−(43)
2.....	Lk Hα 270	250	−(35)	−(42)	−(27)	−(63)	−(29)	−(21)	−(70)	−(27)	−(28)	−(35)	−(180)
3.....	Lk Hα 271	250	−(53)	−(10)	−(12)	−(42)	−(12)	−(8)	880(130)	−(16)	−(19)	−(23)	−(150)
4.....	Lk Hα 326	250	−(39)	−(25)	−(22)	−(110)	−(21)	−(26)	−(88)	−(24)	−(15)	−(33)	−(160)
5.....	Lk Hα 327	250	−(63)	−(60)	−(53)	−(240)	−(64)	−(48)	−(76)	−(59)	−(34)	−(52)	−(48)
6.....	Lk Hα 330	250	−(110)	−(45)	−(27)	−(220)	−(18)	−(34)	−(160)	−(42)	−(100)	−(100)	−(89)
7.....	IRAS 03446+3254	250	−(76)	−(10)	−(6)	−(62)	36(6)	−(13)	−(110)	−(13)	−(44)	−(46)	−(110)
8.....	Lk Ca 8	140	−(22)	−(15)	−(11)	...	−(10)	−(9)	−(71)	−(16)	−(19)	−(27)	−(97)
9.....	IQ Tau	140	−(38)	−(27)	−(24)	...	−(25)	−(23)	−(61)	−(20)	−(18)	−(28)	−(140)
10.....	FX Tau	140	−(37)	−(24)	−(34)	...	−(19)	−(17)	−(97)	−(29)	−(25)	−(19)	−(130)
11.....	V710 Tau	140	−(66)	−(12)	−(12)	...	−(8)	−(11)	−(150)	−(11)	−(28)	−(25)	−(72)
12.....	DN Tau	140	−(33)	−(18)	−(21)	...	−(14)	−(17)	−(77)	−(18)	−(23)	−(31)	−(83)
13.....	CoKu Tau 3	140	−(29)	−(19)	−(14)	...	−(21)	−(16)	450(80)	−(23)	−(26)	−(18)	−(62)
14.....	CoKu Tau 4	140	−(49)	−(30)	−(24)	...	−(10)	−(13)	−(75)	−(33)	−(33)	−(36)	−(87)
15.....	BF Ori	400	−(92)	−(38)	−(48)	−(1000)	−(48)	−(44)	−(73)	−(49)	−(33)	−(180)	−(51)
16.....	RR Tau	160	−(81)	−(52)	−(48)	−(790)	−(63)	−(46)	−(77)	−(52)	−(67)	−(67)	−(73)
17.....	IRAS 08267−3336	400?	−(35)	−(20)	−(22)	−(82)	77(22)	−(22)	−(73)	−(32)	−(26)	−(23)	−(32)
18.....	SX Cha	178	−(46)	−(28)	−(19)	...	−(27)	−(20)	−(54)	−(27)	−(24)	−(30)	−(54)
19.....	SY Cha	178	−(36)	−(13)	−(12)	...	−(12)	−(11)	−(59)	−(21)	−(35)	−(19)	−(44)
20.....	TW Cha	178	−(53)	−(18)	−(14)	...	−(11)	−(16)	−(79)	−(15)	−(27)	−(34)	−(50)
21.....	Ced 110 IRS 6	178	−(66)	−(26)	49(11)	...	50(13)	−(21)	−(60)	−(33)	−(52)	−(47)	−(48)
22.....	B35	178	−(49)	−(11)	−(8)	...	−(4)	−(14)	−(56)	−(10)	−(17)	−(23)	−(48)
23.....	VW Cha	178	−(65)	−(66)	−(57)	...	280(38)	−(55)	−(99)	−(49)	−(30)	−(87)	−(80)
24.....	VZ Cha	178	−(53)	−(23)	−(35)	...	−(26)	−(30)	−(72)	−(22)	−(30)	−(27)	−(43)
25.....	WX Cha	178	−(27)	−(28)	−(22)	...	−(16)	−(26)	580(66)	−(23)	−(46)	−(24)	−(41)
26.....	ISO-ChaI 237	178	−(36)	−(19)	33(9)	...	−(20)	−(15)	−(87)	−(27)	−(31)	−(33)	−(46)
27.....	C7-11	178	−(21)	−(11)	−(8)	...	−(6)	−(11)	470(54)	−(13)	−(32)	−(16)	−(37)
28.....	HM 27	178	−(34)	−(17)	−(12)	...	−(10)	−(21)	−(64)	−(17)	−(43)	−(21)	−(40)
29.....	XX Cha	178	−(34)	−(9)	−(7)	...	35(7)	−(9)	340(81)	−(12)	−(22)	−(20)	−(52)
30.....	HD 98922	>540	−(350)	−(850)	−(840)	...	−(1400)	−(750)	−(600)	−(830)	−(370)	−(450)	−(190)
31.....	HD 101412	160	−(74)	−(89)	−(90)	−(690)	−(120)	−(74)	−(100)	−(110)	−(32)	−(65)	−(66)
32.....	T Cha	66	−(47)	−(17)	−(22)	...	320(21)	−(20)	−(60)	−(29)	−(28)	−(44)	−(50)
33.....	IRAS 12535−7623	178	−(53)	−(15)	−(12)	...	−(13)	−(13)	−(67)	−(18)	−(23)	−(25)	−(46)
34.....	Sz 50	178	−(43)	−(17)	−(14)	...	−(13)	−(13)	−(45)	−(14)	−(40)	−(21)	(70)
35.....	ISO-ChaII 54	178	...	−(12)	−(16)	−(87)	−(13)	−(11)	...	−(24)	...	...	...
36.....	DL Cha	178	−(300)	−(1000)	−(1600)	...	−(2100)	−(1200)	−(410)	−(1100)	−(400)	−(380)	−(140)
37.....	HD 132947	>60	−(2)	−(7)	−(17)	−(86)	−(11)	−(19)	45(6)	−(21)	−(5)	−(3)	−(18)
38.....	HD 135344	140	−(150)	−(51)	−(46)	...	−(32)	−(35)	−(160)	−(67)	−(110)	−(120)	−(160)
39.....	HT Lup	145	−(80)	−(110)	−(47)	−(600)	−(96)	−(75)	−(130)	−(81)	−(78)	−(91)	−(74)
40.....	HT Lup	145	−(160)	−(220)	−(130)	−(1100)	−(120)	−(180)	−(210)	−(240)	−(140)	−(130)	−(110)

TABLE 2—*Continued*

No. (1)	Source (2)	Distance (pc) (3)	H_2 $S(0)$ (4)	H_2 $S(1)$ (5)	H_2 $S(2)$ (6)	H_2 $S(3)$ (7)	[Ne II] (8)	[Ne III] (9)	[Fe I] (10)	[Fe II] 18 μm (11)	[Fe II] 25 μm (12)	[S I] (13)	[Si II] (14)
41.....	GW Lup	100	−(42)	−(10)	−(6)	−(62)	−(7)	−(14)	−(39)	−(27)	−(48)	−(13)	−(31)
42.....	Sz 73	100	−(47)	−(33)	−(35)	−(150)	160(24)	−(35)	−(63)	−(36)	−(37)	−(41)	−(49)
43.....	GQ Lup	100	−(31)	−(36)	−(38)	−(180)	−(27)	−(38)	−(67)	−(46)	−(42)	−(30)	−(69)
44.....	IM Lup	140	−(45)	−(32)	−(20)	−(220)	61(16)	−(27)	−(55)	−(31)	−(34)	−(23)	−(36)
45.....	RU Lup	140	−(110)	−(100)	−(130)	−(720)	−(92)	−(120)	−(120)	−(120)	−(93)	−(150)	−(73)
46.....	RY Lup	150	−(88)	−(55)	−(40)	−(370)	−(32)	−(42)	−(110)	−(110)	−(82)	−(73)	−(89)
47.....	EX Lup	150	−(52)	−(38)	−(33)	−(230)	−(22)	−(40)	−(88)	−(37)	−(45)	−(36)	−(100)
48.....	Sz 102	200	−(35)	32(10)	92(6)	690(56)	360(12)	23(7)	−(49)	49(13)	−(9)	−(9)	−(25)
49.....	AS 205	120	−(250)	−(350)	−(340)	−(2600)	−(270)	−(400)	−(430)	−(390)	−(290)	−(360)	−(150)
50.....	Haro 1−1	125	−(26)	−(24)	−(18)	−(55)	−(17)	−(14)	−(46)	−(22)	−(26)	−(39)	−(52)
51.....	Haro 1−4	125	−(28)	−(35)	−(35)	...	−(21)	−(30)	−(53)	−(37)	−(34)	−(35)	−(61)
52.....	DoAr 24E	125	−(91)	−(140)	−(130)	...	−(120)	−(150)	−(160)	−(180)	−(110)	−(92)	−(100)
53.....	SR 21	125	−(420)	−(220)	−(61)	...	−(100)	−(190)	−(530)	−(390)	−(410)	−(410)	−(270)
54.....	IRS 51	125	−(110)	−(65)	−(30)	...	−(47)	−(36)	−(92)	−(61)	−(96)	−(95)	−(91)
55.....	SR 9	125	−(60)	−(57)	−(42)	...	−(21)	−(32)	−(68)	−(54)	−(38)	−(35)	−(53)
56.....	V853 Oph	125	−(27)	−(26)	−(19)	...	110(21)	−(24)	−(54)	−(30)	−(36)	−(43)	−(63)
57.....	ROX 42C	125	−(37)	−(31)	−(23)	...	−(18)	−(38)	−(41)	−(28)	−(20)	−(39)	−(79)
58.....	ROX 43A	125	−(72)	−(110)	−(74)	...	−(73)	−(91)	−(110)	−(130)	−(47)	−(86)	−(70)
59.....	IRS 60	125	−(30)	−(47)	−(86)	...	140(42)	−(65)	−(62)	−(50)	−(24)	−(75)	−(90)
60.....	Haro 1−16	125	−(48)	−(67)	−(36)	...	−(35)	−(49)	−(110)	−(57)	−(24)	−(73)	−(83)
61.....	Haro 1−17	125	−(33)	−(13)	−(6)	−(59)	16(4)	−(6)	400(88)	−(14)	−(29)	−(20)	−(51)
62.....	RNO 90	140	−(140)	−(190)	−(130)	−(730)	−(94)	−(160)	−(170)	−(160)	−(120)	−(160)	−(110)
63.....	Wa Oph 6	140	−(30)	−(72)	−(56)	−(300)	−(43)	−(54)	−(37)	−(47)	−(16)	−(23)	−(21)
64.....	V1121 Oph	125	−(56)	−(170)	−(120)	−(1600)	−(140)	−(140)	−(89)	−(250)	−(54)	−(81)	−(51)
65.....	HD 163296	122	−(340)	−(610)	−(460)	...	−(440)	−(370)	−(450)	−(720)	−(260)	−(400)	−(170)
66.....	HD 163296	122	−(510)	−(1200)	−(1100)	...	−(400)	−(1200)	−(1200)	−(1100)	−(270)	−(370)	−(350)
67.....	VV Ser	260	−(100)	−(190)	−(170)	−(2000)	−(130)	−(160)	−(120)	−(130)	−(71)	−(76)	−(83)
68.....	SSTc2d J182900.9	260	...	−(32)	−(28)	−(130)	−(16)	−(31)	...	−(37)	...	...	...
69.....	SSTc2d J182909.8	260	...	−(48)	−(43)	−(250)	−(44)	−(35)	...	−(63)	...	...	...
70.....	SSTc2d J182928.2	260	...	−(160)	−(110)	−(1400)	800(120)	−(150)	...	−(260)	...	...	...
71.....	EC 74	260	−(73)	−(12)	46(7)	440(57)	25(6)	−(8)	−(63)	−(12)	−(160)	−(150)	−(130)
72.....	EC 82	260	−(93)	−(100)	170(35)	−(740)	−(63)	−(51)	−(150)	−(130)	−(110)	−(85)	−(120)
73.....	EC 90	260	−(210)	−(410)	−(170)	−(5800)	−(200)	−(310)	−(310)	−(610)	−(250)	−(280)	−(190)
74.....	EC 92	260	−(90)	−(56)	69(18)	−(420)	100(18)	−(38)	−(89)	−(54)	−(48)	−(76)	−(160)
75.....	CK 4	260	−(38)	−(27)	−(19)	−(81)	−(12)	−(23)	−(50)	−(24)	−(18)	−(21)	−(58)
76.....	Lk Hα 348	260	−(48)	−(190)	−(300)	−(2200)	−(220)	−(210)	−(84)	−(560)	−(38)	−(41)	−(30)

NOTE.—Units are 10^{-16} erg cm^{-2} s^{-1}.

(the source flux plus extended emission in the IRS beam) plus an estimate of the extended emission component. Error estimates are derived for both the total emission and the extended emission component. The S/N of the extended emission component can vary significantly depending on the quality of the raw image data and on deviations of the extended emission from the assumed uniformity across the IRS slit. Therefore, care has to be taken when subtracting the extended emission from the total flux signal to retrieve the compact source emission. In some cases, a fit to the extended continuum and line emission is used to avoid adding in surplus noise from the extended emission component. The uncertainty on the fit to the extended emission is propagated into the error of the compact source signal.

3.2. *One-Dimensional Spectra*

After extraction, the one-dimensional spectra are corrected for instrumental fringe residuals (Lahuis & Boogert 2003), order matching is applied, and a pointing flux loss correction is performed to the compact source component. Pointing offsets up to a few arcseconds can have a noticeable impact on the derived fluxes of lines observed with the SH and SL modules, e.g., H_2 0–0 $S(1)$, $S(2)$, [Ne II], and [Ne III]. For example, dispersion offsets within the nominal 3 σ pointing uncertainty of *Spitzer* ($\sim 1''$ for medium accuracy peakup) can lead to SL and SH flux losses up to $\sim$10% depending on wavelength. For all targets, a combination of either the SH, LH, and SL; SH and LH; or SH and SL modules is available. This allows correction of the pointing-related flux losses with an accuracy given by the S/N of the data in the module overlap areas. A detailed description of the c2d pipeline (including extraction, defringing, and pointing flux loss correction) and the c2d legacy products is given in the c2d Spectroscopy Explanatory Supplement (Lahuis et al. 2006b).

3.3. *Spectral Analysis*

The SH and LH modules of the IRS instrument cover the positions of the three lowest pure rotational lines of H_2 and emission of [Ne II] (12.8 μm), [Ne III] (15.55 μm), [Fe I] (24 μm), [Fe II] (17.9 and 26.0 μm), [S I] (25.25 μm), [S III] (18.7 μm), and [Si II] (34.8 μm) at a resolving power of $R = \lambda/\Delta\lambda = 600$. Line fitting and flux integration is done using routines from OSIA.[6]

As discussed in § 3.1, the extended emission component, both in the continuum and the spectral line, is subtracted from the spectrum prior to line fitting. Uncertainty estimates, as listed in Table 2, are derived from the residuals after line fitting or, in the absence of a spectral line, using the line width derived from the instrumental resolution. The uncertainty derived from the extended emission is added into the uncertainty estimate of the source component. As a result, the 1 σ uncertainty estimates can vary widely for sources with a similar continuum flux and integration time. This may for example be the result of the presence of artifacts resulting from hot pixels or small variations in the extended emission that are not accounted for in the spectral extraction, which assumes a constant extended emission component.

Typical mean 3 σ uncertainties prior to subtraction of the extended component for the high-resolution modules range from $\sim 1 \times 10^{-16}$ to 2×10^{-15} erg cm^{-2} s^{-1} with positive and negative extremes of $\sim 5 \times 10^{-17}$ and $\sim 1 \times 10^{-14}$ erg cm^{-2} s^{-1}. The uncertainties are comparable to those from Pascucci et al. (2006) for FEPS observations using on-source integration times similar to those used for the c2d sample.

[6] OSIA is a joint development of the *ISO* SWS consortium. Contributing institutes are SRON, MPE, KUL, and the ESA Astrophysics Division. See http://sws.ster.kuleuven.ac.be/osia/.

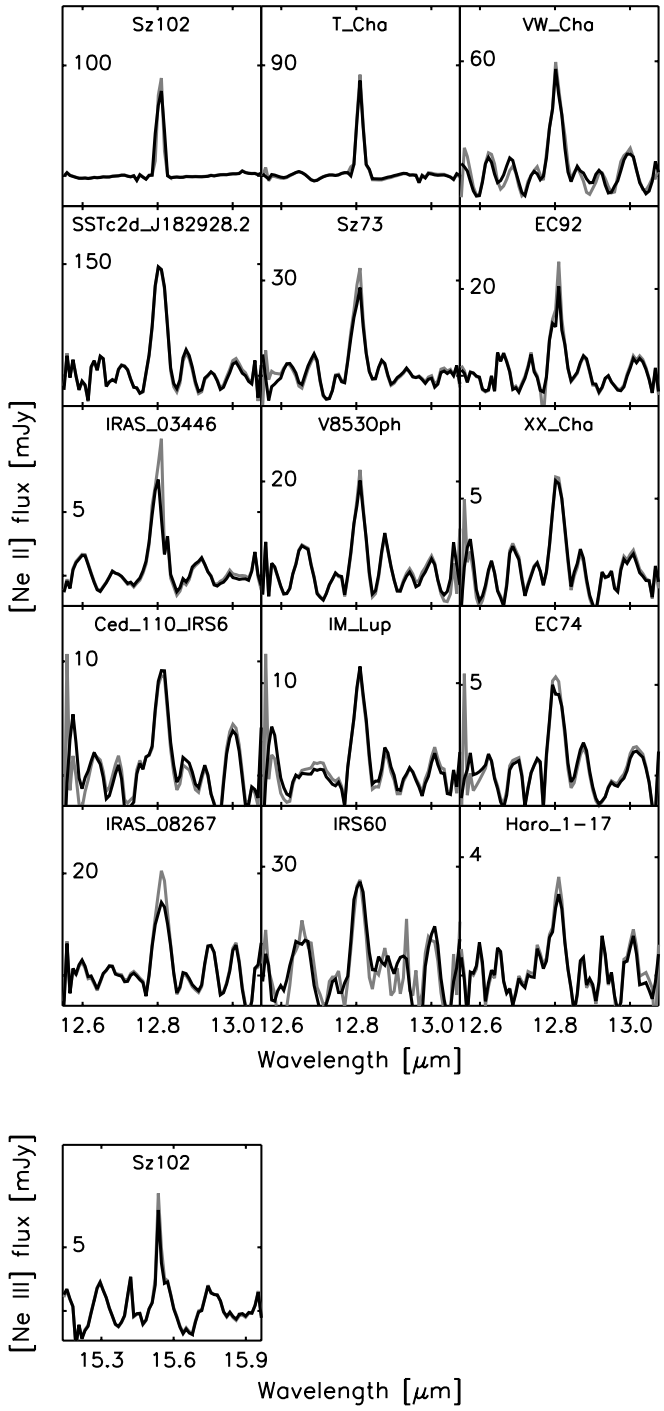

FIG. 3.—Detections of neon lines at the 3 σ level or more toward the c2d sample of T Tauri stars with disks. Of all the H_2 and atomic fine-structure lines [Ne II] is most convincingly detected toward $\sim$20% of the sources. Plotted is the total observed emission (compact source + extended component, *gray lines*) and the emission after correction of the estimated sky component (*black lines*). None of the sources show a significant extended component.

4. RESULTS

4.1. *Atomic Fine-Structure Lines: Neon*

Of all the atomic fine-structure lines covered by the SH and LH modules, the [Ne II] 12.8 μm transition is most convincingly detected and shows the strongest source emission. The higher

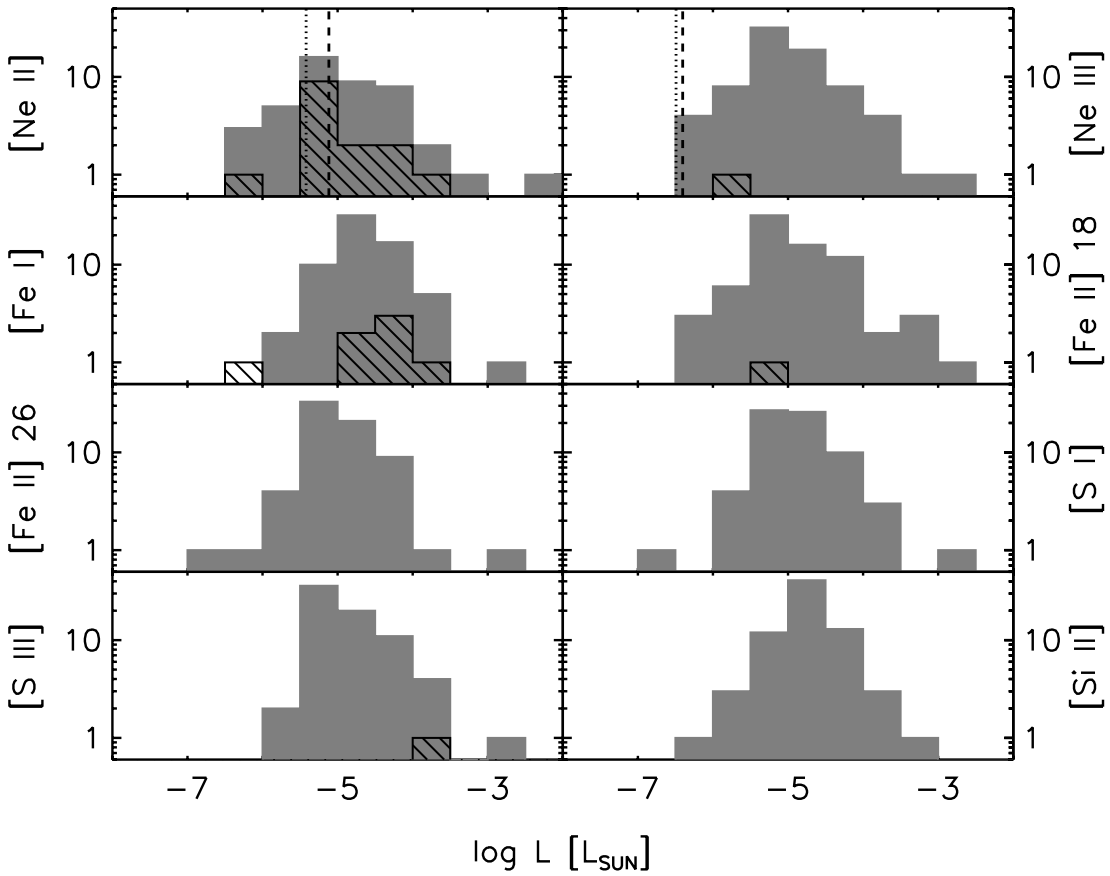

FIG. 4.—Observed line strengths (*hatched bars*) and upper limits (*solid gray bars*) of the major atomic lines. Included with vertical lines are model-predicted line strengths for [Ne II] and [Ne III] by Glassgold et al. (2007). The model incorporates UV and X-ray heating of the circumstellar disk. The two lines represent two extreme thermal models, X-ray heating dominant (*dotted line*) or mechanical heating dominant (*dashed line*).

excitation [Ne III] 15.5 μm line is tentatively detected toward Sz 102 but not toward any of the other sources in our sample. Figure 3 shows all [Ne II] and [Ne III] lines detected at 3 σ or more; see also Figure 1 of Geers et al. (2006) for the [Ne II] 12.8 μm line toward T Cha. Plotted in Figure 3 is the total continuum-subtracted observed [Ne II] emission (*gray lines*) and the compact source emission after correction for extended line emission (*black lines*). Taken together, [Ne II] emission is observed in the spectra of 15 T Tauri sources ($\sim$20% of the sample). These are the first reported detections of [Ne II] toward disks around classical T Tauri stars. The optimal extraction method, together with the limited minimaps (§ 2.2 and Fig. 1), shows that the emission is indeed associated with the source itself.

The observed line fluxes and upper limits of [Ne II] and [Ne III] are listed in columns (8) and (9) of Table 2. When line fluxes are compared (observed or with models) the line strength is converted to solar luminosities since the sample is observed toward sources from multiple clouds and compared to model predictions using different assumed distances. Figure 4 shows the distribution of the observed line strengths (*hatched bars*) and upper limits (*solid gray bars*).

4.2. *Atomic Fine-Structure Lines: Other Species*

[Fe I] at 24 μm is the only other species besides [Ne II] with clear detections toward seven sources ($\sim$9% of the sample). Of the other atomic lines there is one detection of [Fe II] at 18 μm and one of [S III] at 18.7 μm, in different sources. [S I] at 25 μm, [Fe II] at 26 μm, and [Si II] at 34 μm are not detected. The derived line fluxes and upper limits are listed in columns (9)–(14) of Table 2. The detected lines are plotted in Figure 5, whereas Figure 4 shows the distribution of the observed line strengths.

4.3. *Molecular Hydrogen*

H_2 emission is detected toward a small number of sources. Figure 6 shows the observed H_2 0–0 $S(2)$ and $S(3)$ emission lines detected at 3 σ or more. The total (compact and extended line emission) observed H_2 emission (*gray lines*) and the emission after subtraction of the extended line emission (*black lines*) are shown. The H_2 0–0 $S(0)$ and $S(1)$ lines are seen toward some sources such as HD 132947 and Sz 102 (Fig. 1) but they are found to be mostly extended. Only for Sz 102 is compact source emission of H_2 0–0 $S(1)$ tentatively detected. Neither $S(0)$ nor $S(1)$ is seen toward HD 135344 and HD 163296. The 3 σ upper limits for HD 135344 are a factor of $\sim$2–3 lower than the tentative detections in Thi et al. (2001), while for HD 163296 the upper limits are comparable to the *ISO* SWS line fluxes. The observed line fluxes and upper limits of the H_2 0–0 $S(0)$, $S(1)$, $S(2)$, and $S(3)$ emission lines are listed in columns (4)–(7) of Table 2. Figure 7 shows the distribution of observed line strengths (*hatched bars*) and upper limits (*solid gray bars*) of H_2 0–0 $S(0)$, $S(1)$, $S(2)$, and $S(3)$.

In the simplest analysis, the H_2 excitation is assumed to be in local thermal equilibrium (LTE; e.g., Thi et al. 2001) with an ortho-to-para ratio determined by the kinetic temperature of the gas (following Sternberg & Neufeld 1999). For gas temperatures

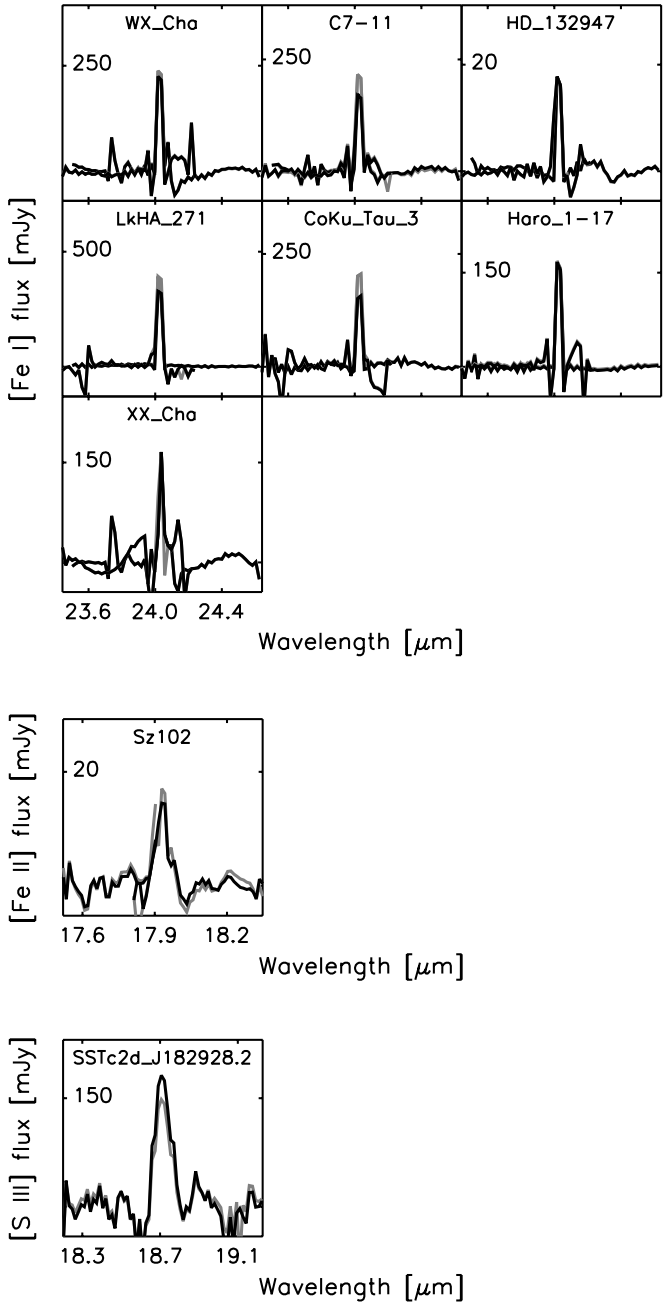

FIG. 5.—Detections of [Fe I], [Fe II], and [S III] toward the c2d sample of T Tauri stars with disks. Plotted is the total observed emission (compact source + extended emission, *gray lines*) and the emission after correction of the estimated extended component (*black lines*). No significant extended line emission is observed.

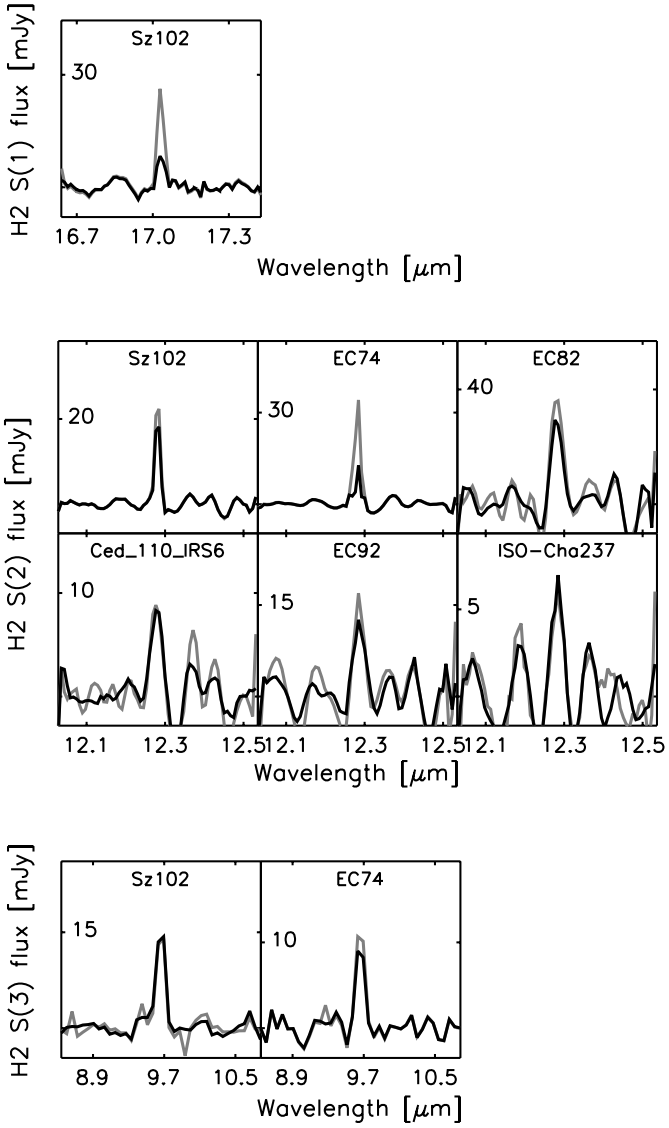

FIG. 6.—Detection of H_2 lines toward the c2d sample of T Tauri stars with disks. Only a few of the 76 sources show clear detections. Plotted is the total observed emission (compact source + extended component, *gray lines*) and the emission after correction of the estimated extended emission (*black lines*).

100, 150, and $\geq$200 K, the ortho-to-para ratios are 1.6, 2.5, and 3, respectively. Assuming optically thin emission, the integrated flux of a rotational line $J_u \rightarrow J_l$ for a given temperature $T_{\rm ex}$ is

$$F_{ul} = \frac{hc}{4\pi\lambda} N_{\rm H_2} A_{ul} x_u \Omega \text{ erg s}^{-1} \text{ cm}^{-2}, \quad (1)$$

where λ is the wavelength of the transition, $N_{\rm H_2}$ the total column density, A_{ul} the spontaneous transition probability, and Ω the source size. For high enough densities ($n \gtrsim 10^3$ cm^{-3}), the population x_u follows the Boltzmann law,

$$x_u = \frac{g_N (2J_u + 1) e^{-E_J/kT_{\rm ex}}}{Q(T_{\rm ex})}, \quad (2)$$

where E_J is the energy of the upper level, g_N is the nuclear statistical weight (1 for para and 3 for ortho H_2), and $Q(T_{\rm ex})$ is the partition function for the given excitation temperature $T_{\rm ex}$.

We can use the above equations to derive excitation temperatures, column densities, and H_2 gas masses from the observed line fluxes and upper limits. If either $S(0)$ or $S(1)$ is detected an upper or lower limit on the temperature of the warm gas is derived, but if neither is detected a temperature of 100 K is assumed for the warm gas. If two or more higher excitation lines [$S(2)$ and higher] are detected a temperature for the hot component is derived, while if no or only one of the higher excitation lines is detected a temperature of 1000 K is assumed. For Sz 102 and EC 74 temperatures of $T_{\rm hot} \sim 700$–800 K could be found for the hot component. For all other sources no temperatures could be derived for either component.

The column density averaged over the IRS aperture can be derived from the above equations, given the distance to the source. For all sources in our sample the emitting source size in the disk is smaller than the IRS aperture (§ 3.1), and since this is unknown a typical emitting disk region is assumed. For the warm component

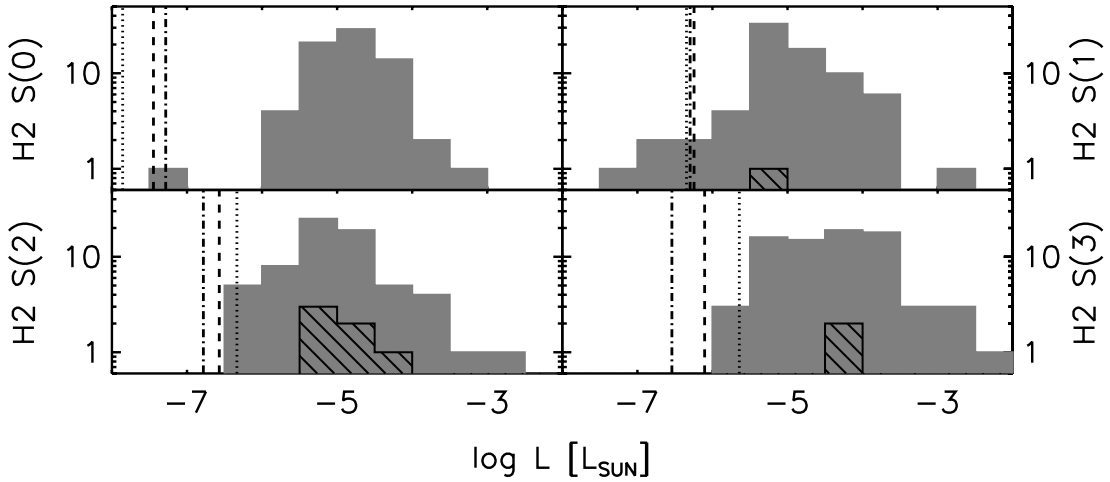

FIG. 7.—Observed line strengths (*hatched bars*) and upper limits (*solid gray bars*). The vertical lines present model T Tauri disk line strengths of H_2 $S(0)$, $S(1)$, $S(2)$, and $S(3)$ from Nomura et al. (2007). The models incorporate UV and X-ray heating of the circumstellar disk for three grain size distributions ($a_{max} = 10$ μm, 1 mm, and 10 cm, *dotted, dashed, and dash-dotted lines, respectively*). For $S(0)$ the line strength increases with increasing maximum grain size, while for $S(2)$ and $S(3)$ the line strength decreases as the maximum grain size increases.

a source with a radius $r = 100$ AU is assumed and for the hot component a source with a radius $r = 2$ AU. The derived or assumed temperature plus the (upper level) column densities give a total column density, which in turn gives the total H_2 gas mass in Jovian masses, $M = (\pi r^2 N)2m_H/M_J$, with $m_H = 1.674 \times 10^{-24}$ g and $M_J = 1.9 \times 10^{30}$ g.

The derived H_2 parameters for both the warm and hot gas components are listed in Table 3. Figure 8 shows the distribution of the derived H_2 masses for the assumed temperatures of 100 and 1000 K, respectively.

4.4. *Correlations*

Figure 9 shows the observed line strengths and upper limits of H_2 0–0 $S(2)$, [Ne II], and [Fe I] as functions of the mid-IR luminosities (in solar luminosities), the 12.8–26 μm spectral index, and the effective temperature. The mid-IR luminosity is integrated using the 12.8 and 15.5 μm continuum points derived in the [Ne II] (12.8 μm) and [Ne III] (15.5 μm) spectral line fits. The effective temperature is derived from the stellar type (Gray & Corbally 1994; Baraffe & Chabrier 1996). In all panels the sources with H_2 0–0 $S(2)$, [Ne II], or [Fe I] detections are plotted with large black symbols, whereas the sources without line detections are plotted with small gray symbols.

The line strength plots as a function of the mid-IR luminosity clearly show the detection limits of the *Spitzer* IRS instrument with an obvious increase of the upper limits with increasing continuum. Therefore, no definite conclusions can be drawn about the apparent correlations, and the detection rate could be increased significantly with higher S/N for strong continuum sources. However, the plots do show that there are no low-luminosity sources with strong H_2 0–0 $S(2)$ or [Ne II] emission. No correlation with the 12.8–26 μm spectral index is observed. The detections are distributed over a range of spectral indices, illustrating that the line detections are not limited to a single type of disk source (e.g., flat or flaring).

The correlation with the effective temperature shows a differentiation between [Ne II] and [Fe I] compared with H_2 0–0 $S(2)$. The [Ne II] and [Fe I] line strengths show a similar correlation with effective temperature as with the mid-IR luminosity, but with more scatter. In addition, upper limits are seen below the correlation line for sources with detections. There are a few detected sources deviating from the observed trend, such as the cold disk source T Cha (see Brown et al. 2007) detected in [Ne II] and the Herbig Ae star HD 132947 detected in [Fe I]. T Cha is located at a distance of 66 pc, much closer than the majority of sources in our sample. Sources with a similar [Ne II] line strength to that of T Cha but at the distances of the nearest star-forming clouds would go undetected at the sensitivity limits of the current sample. For HD 132947 the distance is unknown, and the assumed distance of 60 pc is the lower limit from Tycho. The H_2 0–0 $S(2)$ line, although detected for only a small number of sources, differs from [Ne II] and [Fe I] in that all sources are concentrated around a single effective temperature. This may be real, but it could also be the result of a S/N selection. More sensitive observations will be required to draw firm conclusions.

5. DISCUSSION

The most significant outcome of this survey is the detection of [Ne II] emission toward 15 T Tauri stars, ~20% of the sample. [Fe I] is also seen toward seven sources, ~9% of the sample (see §§ 4.1 and 4.2).

5.1. [Ne II]

Since neon cannot be ionized by photons with energies less than 21.4 eV (and Ne^+ 41.0 eV), the detection of [Ne II] is evidence for the presence of higher energy photons in the circumstellar environment, specifically extreme-UV (EUV) photons or X-rays originating from either the stellar chromosphere or (accretion) shocks. Alternatively, high-velocity shocks can result in ionized lines.

5.1.1. *X-Ray Emission*

T Tauri stars are known to be strong emitters of moderately hard X-rays. Feigelson & Lawson (2004) report X-ray luminosities toward young stars in the Chamaeleon I North cloud of $L_X = 10^{28}$–10^{30} erg s^{-1}, whereas Telleschi et al. (2007) find X-ray luminosities toward young stars in the Taurus molecular clouds of $L_X = 10^{28}$–10^{31} erg s^{-1} with a clear stellar mass dependence. A number of sources in our sample have been identified with X-ray sources and have derived X-ray luminosities varying from $L_X \sim 4 \times 10^{28}$ to 10^{31} erg s^{-1} (Table 4).

TABLE 3

DIAGNOSTIC PARAMETERS OF THE DISK GAS CONTENTS

No.[a] (1)	Source (2)	T_{warm}[b] (K) (3)	N_{warm}[b] ($r = 100$ AU)[c] (10^{22} cm^{-2}) (4)	M_{warm}[b] (M_J) (5)	T_{hot}[b] (K) (6)	N_{hot} ($r = 2$ AU)[c] (10^{22} cm^{-2}) (7)	M_{hot} (10^{-3} M_J) (8)
1	RNO 15	...	<74	<9.2	...	<75	<3.7
2	Lk Hα 270	...	<59	<7.3	...	<18	<0.9
3	Lk Hα 271	...	<35	<4.3	...	<16	<0.8
4	Lk Hα 326	...	<44	<5.5	...	<37	<1.9
5	Lk Hα 327	...	<86	<10.6	...	<80	<4.0
6	Lk Hα 330	...	<110	<13.0	...	<72	<3.5
7	IRAS 03446+3254	...	<43	<5.3	...	<30	<1.5
8	Lk Ca 8	...	<8	<1.0	...	<4	<0.2
9	IQ Tau	...	<15	<1.8	...	<9	<0.5
10	FX Tau	...	<13	<1.6	...	<13	<0.7
11	V710 Tau	...	<14	<1.7	...	<4	<0.2
12	DN Tau	...	<11	<1.4	...	<8	<0.4
13	CoKu Tau 3	...	<11	<1.3	...	<5	<0.3
14	CoKu Tau 4	...	<18	<2.2	...	<9	<0.5
15	BF Ori	...	<220	<26.8	...	<225	<11.2
16	RR Tau	...	<32	<4.0	...	<155	<7.7
17	IRAS 08267−3336	...	<98	<12.2	...	<77	<3.9
18	SX Cha	...	<27	<3.4	...	<12	<0.6
19	SY Cha	...	<16	<2.0	...	<7	<0.4
20	TW Cha	...	<24	<2.9	...	<9	<0.4
21	Ced 110 IRS 6	...	<32	<3.9	...	<10	<0.5
22	B35	...	<18	<2.2	...	<5	<0.3
23	VW Cha	...	<48	<5.9	...	<37	<1.9
24	VZ Cha	...	<26	<3.2	...	<22	<1.1
25	WX Cha	...	<20	<2.5	...	<15	<0.7
26	ISO-ChaI 237	...	<20	<2.5	...	<7	<0.4
27	C7-11	...	<12	<1.4	...	<5	<0.3
28	HM 27	...	<18	<2.3	...	<7	<0.4
29	XX Cha	...	<14	<1.7	...	<4	<0.2
30	HD 98922	...	<2200	<274.3	...	<11000	<546.2
31	HD 101412	...	<40	<4.9	...	<110	<5.4
32	T Cha	...	<2	<0.4	...	<1	<0.1
33	IRAS 12535−7623	...	<22	<2.7	...	<7	<0.4
34	Sz 50	...	<21	<2.5	...	<8	<0.4
35	ISO-ChaII 54	...	<6	<0.8	...	<14	<0.7
36	DL Cha	...	<200	<24.3	...	<1975	<98.5
37	HD 132947	...	<0.2	<0.0	...	<1	<0.1
38	HD 135344	...	<41	<5.1	...	<18	<0.9
39	HT Lup	...	<42	<5.1	...	<47	<2.4
40	HT Lup	...	<84	<10.4	...	<75	<3.8
41	GW Lup	...	<4	<0.6	...	<4	<0.2
42	Sz 73	...	<9	<1.1	...	<8	<0.4
43	GQ Lup	...	<7	<0.9	...	<8	<0.4
44	IM Lup	...	<17	<2.1	...	<12	<0.6
45	RU Lup	...	<47	<5.8	...	<52	<2.6
46	RY Lup	...	<37	<4.5	...	<23	<1.1
47	EX Lup	...	<23	<2.9	...	<17	<0.9
48	Sz 102	...	<17	<2.1	970	27	1.4
49	AS 205	...	<89	<11.1	...	<117	<5.9
50	Haro 1–1	...	<8	<1.1	...	<7	<0.3
51	Haro 1–4	...	<9	<1.1	...	<19	<0.9
52	DoAr 24E	...	<30	<3.8	...	<87	<4.4
53	SR 21	...	<120	<14.7	...	<19	<1.0
54	IRS 51	...	<32	<3.9	...	<9	<0.5
55	SR 9	...	<21	<2.7	...	<14	<0.7
56	V853 Oph	...	<9	<1.1	...	<9	<0.5
57	ROX 42C	...	<13	<1.6	...	<7	<0.4
58	ROX 43A	...	<26	<3.2	...	<52	<2.5
59	IRS 60	...	<9	<1.2	...	<37	<1.8
60	Haro 1–16	...	<18	<2.2	...	<24	<1.2

TABLE 3—*Continued*

No.[a] (1)	Source (2)	T_{warm}[b] (K) (3)	N_{warm}[b] ($r = 100$ AU)[c] (10^{22} cm^{-2}) (4)	M_{warm}[b] (M_J) (5)	T_{hot}[b] (K) (6)	N_{hot} ($r = 2$ AU)[c] (10^{22} cm^{-2}) (7)	M_{hot} (10^{-3} M_J) (8)
61	Haro 1–17	...	<7	<1.0	...	<3	<0.1
62	RNO 90	...	<70	<8.7	...	<62	<3.1
63	Wa Oph 6	...	<19	<2.3	...	<25	<1.3
64	V1121 Oph	...	<33	<4.0	...	<37	<1.9
65	HD 163296	...	<120	<14.4	...	<300	<15.1
66	HD 163296	...	<170	<21.1	...	<725	<36.3
67	VV Ser	...	<150	<19.2	...	<500	<25.3
68	SSTc2d J182900.9	...	<53	<6.5	...	<40	<2.0
69	SSTc2d J182909.8	...	<67	<8.3	...	<95	<4.7
70	SSTc2d J182928.2	...	<340	<42.3	...	<167	<8.3
71	EC 74	...	<48	<5.9	974	27	1.3
72	EC 82	...	<150	<18.1	...	<137	<6.8
73	EC 90	...	<340	<42.1	...	<875	<43.4
74	EC 92	...	<110	<13.7	...	<80	<4.0
75	CK 4	...	<51	<6.3	...	<32	<1.6
76	Lk Hα 348	...	<71	<8.8	...	<675	<33.0

[a] Source number from Tables 1 and 2.
[b] 100 K is assumed for the warm component and 1000 K for the hot component. The derived column density and mass of the warm component depend strongly on the assumed temperature. A temperature of 150 and 200 K reduces the column density and mass by a factor of ~30 and 140, respectively. For the hot component, 1500 K instead of 1000 K may result in a reduction of column density and mass up to a factor of 10.
[c] For the unresolved emission a source with $r = 50$ AU is assumed to obtain an estimate of the column density.

Recently Glassgold et al. (2007) modeled the excitation of neon in an X-ray irradiated flaring disk model according to D'Alessio et al. (1999) and predicted [Ne II] and [Ne III] line intensities. For a source at 140 pc (the assumed distance in Glassgold et al. 2007) [Ne II] line fluxes of $(0.6–1) \times 10^{-14}$ erg cm^{-2} s^{-1} and [Ne III] line fluxes of $(5–6.5) \times 10^{-16}$ erg cm^{-2} s^{-1} are predicted. The predicted [Ne II] line strength of $\sim(4–8) \times 10^{-6}$ $L_\odot$ falls within the observed range of line strengths (see Table 4). The predicted [Ne III] line strength is at the lower end of the *Spitzer* IRS [Ne III] upper limits. Interestingly the predicted [Ne II] line strength agrees well at 4000 K (the assumed effective temperature in the Glassgold et al. [2007] model) with the trend in the observed line strengths as shown in Figure 9. In addition, the [Ne II]/[Ne III] line ratio for Sz 102 agrees with the line ratios from the Glassgold et al. (2007) model.

The Glassgold et al. (2007) model is based on an assumed neon abundance of 10^{-4} and an X-ray luminosity and spectral temperature of $L_X = 2 \times 10^{30}$ erg s^{-1} and $kT_X = 1$ keV, respectively, appropriate for solar-mass pre–main-sequence stars observed in Orion (Wolk et al. 2005). Lower mass, older, and accreting stars may have a lower X-ray luminosity (e.g., Feigelson & Lawson 2004; Preibisch et al. 2005; Telleschi et al. 2007) leading to lower expected line intensities, whereas higher X-ray luminosities, higher neon abundances (Drake et al. 2005; Cunha et al. 2006), or the inclusion of H atom collisions (not included in the Glassgold et al. [2007] calculations) may yield higher predicted line intensities. The neon line fluxes also scale with the disk mass surface density and are therefore sensitive to the disk geometry, e.g., flaring or nonflaring disks.

Of the sources with [Ne II] emission about 30% are identified as X-ray sources. The remaining sources may have escaped detection due to incomplete or sensitivity limited X-ray searches or due to source geometry prohibiting the detection of the X-rays. A more targeted deep X-ray search would be required to confirm a direct relation between observed [Ne II] emission and X-ray luminosities. Overall, variations in X-ray luminosities, age, stellar mass, and geometry appear able to cover the 2–3 orders of magnitude range in the observed [Ne II] line fluxes.

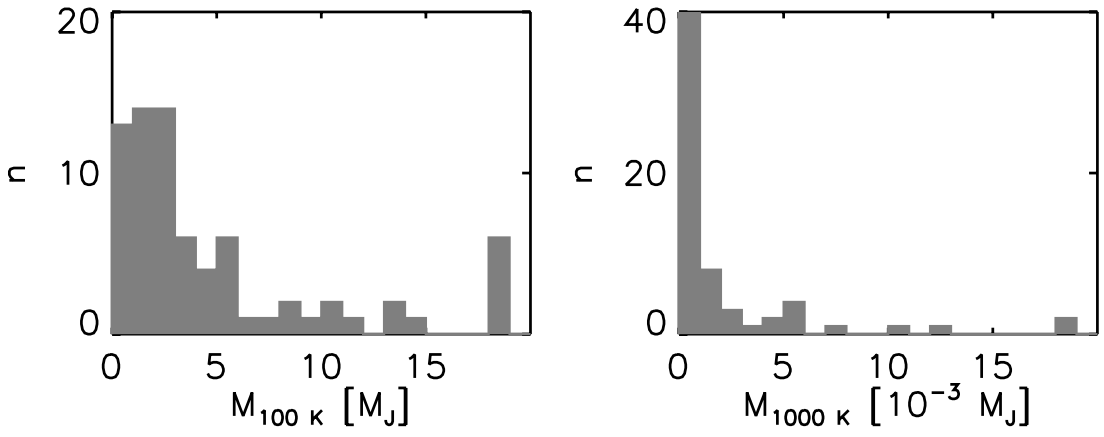

FIG. 8.—Distribution of H_2 mass upper limits derived for 100 and 1000 K gas.

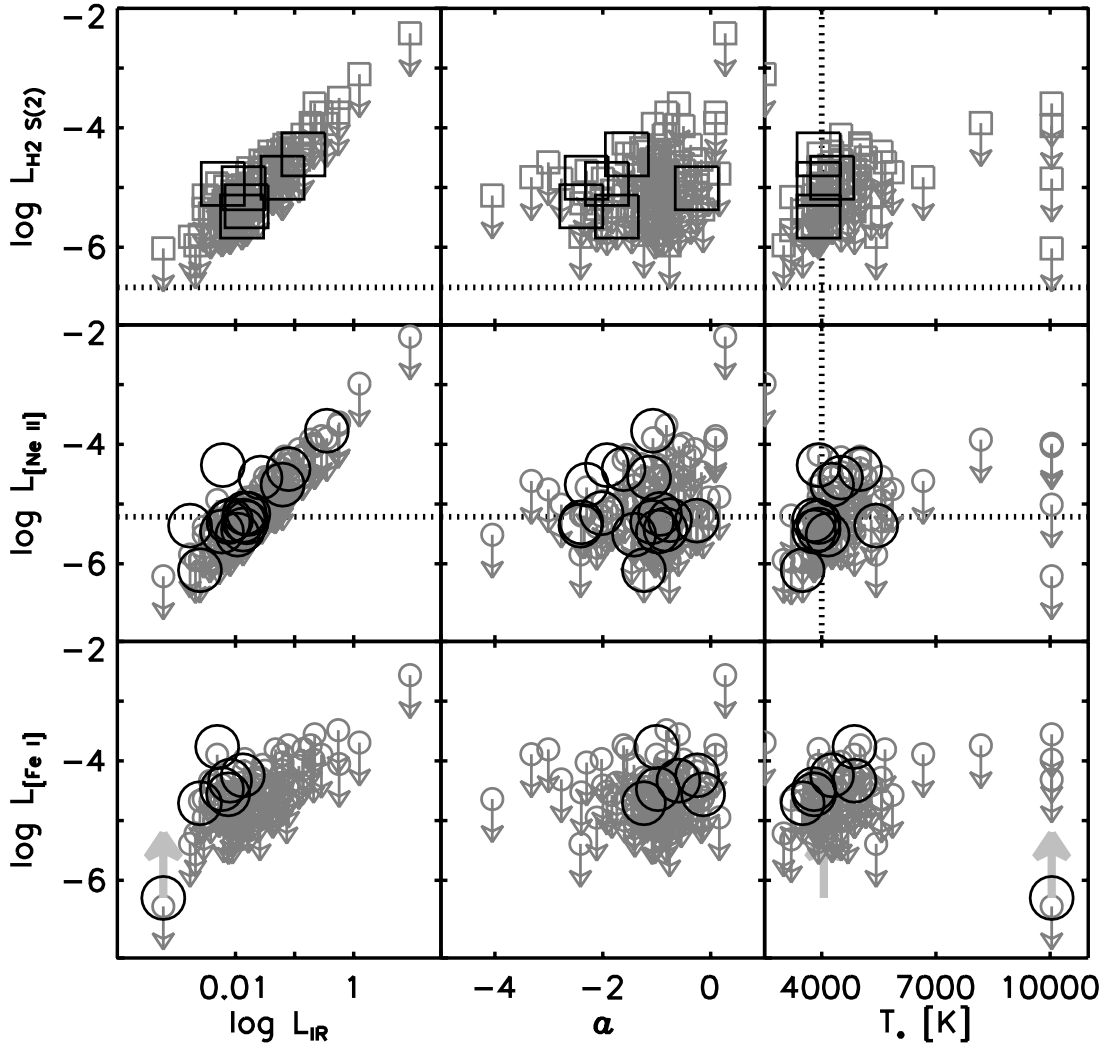

FIG. 9.—Comparison of the observed H_2 $S(2)$, [Ne II], and [Fe I] line strengths in solar luminosities with the mid-IR luminosity, the 12.8–26 μm spectral index, and the effective temperature of the sources. Plotted with the large black symbols are the line detections, while the small gray symbols and arrows are all nondetections. The horizontal dotted lines in the H_2 and [Ne II] panels show the predicted line strength by Nomura et al. (2007) and Glassgold et al. (2007), who use an effective temperature of 4000 K in their models. The vertical dotted lines mark 4000 K.

5.1.2. *Extreme-UV Radiation*

EUV radiation originating from the stellar chromosphere or the accretion shock may be an additional heating component of the disk surface and contribute to the neon excitation. EUV photons, however, are quickly absorbed by atomic hydrogen in the accretion column (Alexander et al. 2005) and for strong accretors will not reach the disk surface. However, for transitional objects such as T Cha the accretion column can become optically thin to EUV photons and some EUV radiation may escape the immediate surroundings of the star and reach the disk surface, potentially contributing to the ionizing radiation at the factor of 2 level. The [Ne II]/[Ne III] ratio is expected to increase with the additional EUV contribution given the high (41.0 eV) ionization potential of Ne^+. For Sz 102 the tentative [Ne III] detection results in a [Ne II]/[Ne III] ratio consistent with X-ray excitation. For all other sources, however, the [Ne III] upper limits do not put any constraints on this (see Fig. 10).

5.1.3. *Disk Shocks*

The presence of strong [Ne II] could also indicate a possible origin of the observed [Ne II] emission induced by shocks in the disk. Hartmann & Raymond (1989) describe shocks resulting from the stellar wind striking the disk surface at an oblique angle. For typical wind velocities of 200 km s^{-1} shock velocities along the disk surface are estimated to be ~30–40 km s^{-1}. For such shocks and a medium with a density of 10^5–10^6 cm^{-3}, Hollenbach & McKee (1989) predict [Ne II] line strengths of $\sim 10^{-6}$ to 10^{-4} erg cm^{-2} s^{-1} sr^{-1}. For a 100 AU disk at 100 pc, the upper end of this range implies a [Ne II] line flux of approximately 10^{-14} erg cm^{-2} s^{-1}, of the same order as that observed. However, Hollenbach & McKee (1989) also predict the H_2 0–0 $S(1)$, $S(2)$, and $S(3)$ lines and the [Fe I] 24 μm, [S I] 25.25 μm, [Fe II] 26 μm, and [Si II] 34.8 μm spectral lines to be stronger than the [Ne II] line by 1–3 orders of magnitude for these velocities, as illustrated in the bottom right plot of Figure 10. The top plots of Figure 10 show the observed ratios and lower limits. For almost all of the line pairs, the ratios are roughly equal to or larger than unity, except for a small number of cases.

To account for line ratios equal to or larger than unity, higher velocity shocks would be required. At high shock velocities ($v \gtrsim$ 70 km s^{-1}) and high densities ($\gtrsim 10^5$ cm^{-3}) the J-type shock models presented in Hollenbach & McKee (1989) give [Ne II], [Fe I] 24 μm, [S I] 25.25 μm, [Fe II] 26 μm, and [Si II] 34.8 μm lines all

TABLE 4
SUMMARY OF DATA FOR SOURCES WITH DETECTED H_2, [Ne II], OR [Fe I] EMISSION

No.	Source	log L ($L_\odot$)					T_*	Age	Class	log L_X	L_X Ref.
		H_2 $S(2)$	H_2 $S(3)$	[Ne II]	[Fe I]	IR	(K)	(Myr)		(erg s^{-1})	
27	C7-11	<−5.6	...	<−5.7	−4.3	−2.1	4860	0.6	TTs	...	...
21	Ced 110 IRS 6	−5.3	...	−5.3	<−4.8	−1.8	...	...	1	28.6	1
13	CoKu Tau 3	<−5.6	...	<−5.4	−4.6	−2.1	3800	...	CTTs	30.8	2
71	EC 74	−5.0	−4.0	−5.3	<−4.4	−1.9	...	...	2	30.5	3
72	EC 82	−4.4	<−3.3	<−4.4	<−4.0	−0.9	3918	...	TTs	...	...
74	EC 92	−4.8	<−3.6	−4.7	<−4.3	−1.2	4273	...	TTs	...	...
37	HD 132947	<−6.2	<−5.5	<−6.4	−6.3	−3.2	10040	...	HAeBe	...	...
61	Haro 1–17	<−6.0	<−5.1	−6.1	−4.7	−2.6	3500	...	TTs	...	...
44	IM Lup	<−5.4	<−4.4	−5.4	<−5.0	−1.9	3918	0.7	TTs	...	...
7	IRAS 03446+3254	<−5.4	<−4.4	−5.2	<−4.2	−2.0	...	...	TTs	...	...
17	IRAS 08267−3336	<−4.5	<−3.9	−4.4	<−4.0	−1.1	5010	2.0	TTs	...	...
59	IRS 60	<−4.9	...	−5.2	<−5.0	−1.8	...	...	...	...	...
26	ISO-ChaI 237	−5.5	...	<−5.2	<−4.6	−1.9	3918	...	TTs	29.2	4
3	Lk Hα 271	<−5.2	<−4.6	<−5.2	−3.8	−2.3	4860	...	TTs	...	...
55	SR 9	<−5.2	...	−5.5	<−5.0	−2.0	4155	0.8	TTs	...	...
70	SSTc2d J182928.2	<−4.2	<−3.1	−3.8	...	−0.5	...	...	...	...	...
48	Sz 102	−4.9	−4.1	−4.3	<−4.7	−2.2	3918	...	TTs	28.6	5
42	Sz 73	<−5.5	<−4.9	−5.3	<−5.2	−2.1	3918	3.7	TTs	...	...
32	T Cha	<−6.0	...	−5.4	<−5.6	−2.8	5430	2.1	TTs	30.1	6
56	V853 Oph	<−5.6	...	−5.3	<−5.1	−2.1	3800	0.8	TTs	...	...
23	VW Cha	<−4.8	...	−4.6	<−4.5	−1.6	4510	1.2	CTTs	31.0	7
25	WX Cha	<−5.2	...	<−5.3	−4.2	−1.9	4273	2.3	TTs	30.2	7
29	XX Cha	<−5.7	...	−5.5	−4.5	−2.2	3800	14.6	TTs	...	...

REFERENCES.—(1) Carkner et al. 1998; (2) Audard et al. 2007; (3) Preibisch 2003; (4) Feigelson & Lawson 2004; (5) Gondoin 2006; (6) Alcala et al. 1997; (7) Stelzer et al. 2004.

of comparable strength of $\sim$0.004 erg cm^{-2} s^{-1} sr^{-1} (see Fig. 10, *bottom right*). To produce a line flux of $\sim 10^{-14}$ erg cm^{-2} s^{-1} the shocked emission would have to come from a region of the disk with a radius of $\sim$10 AU at a distance of 100 pc. Higher velocity shocks may produce the observed line flux ratios and lower limits, but a possible origin for such high-velocity shocks is unclear. Another problem lies in the nondetection of the [S I] 25.25 μm, the [Fe II] 26 μm, and the [Si II] 34.8 μm lines. In particular the [S I] line should be detected if high-velocity shocks are the origin of the observed line emission: the [S I] line is predicted to be stronger, whereas the detection limits for [Fe I] and [S I] are comparable in our data (see Fig. 4).

5.2. [Fe I] *and* [S I]

As mentioned in § 5.1 the detection of [Fe I] in combination with the nondetection of other atomic lines, in particular [S I] and [Si II], is significant.

Gorti & Hollenbach (2004) modeled the line emission from intermediate-aged optically thin disks around G and K stars. For disks with low gas masses (10^{-3} to 10^{-2} M_J), the [S I] 25.2 μm, [Fe II] 26 μm, and [Si II] 35.4 μm lines are expected to be the strongest mid-infrared emission lines. However, as the disk mass increases a larger fraction of the sulfur turns molecular and the [Si II] and [Fe II] emission becomes optically thick. At the same time the [Fe I] lines are predicted to become increasingly stronger and will at some point, around 0.1 M_J, dominate over the [S I] emission. Although specific calculations for these optically thick disks are lacking, the seven sources (WX Cha, C7-11, HD 132947, Lk Hα 271, CoKu Tau 3, Haro 1–17, and XX Cha) which show strong [Fe I] emission may well have optically thick massive gas-rich disks.

5.3. *Molecular Hydrogen*

The third significant result of our survey is the nondetection of the H_2 0–0 $S(0)$ and $S(1)$ lines for 76 T Tauri and Herbig Ae/Be stars. This puts constraints on the mass of warm ($T \sim$ 100–200 K) H_2 gas in the disks around these stars of typically a few Jovian masses as illustrated in Figure 8. Models of disk heating by stellar UV photons show that the gas temperature in the surface layers can be significantly higher than that of the dust down to an optical depth for UV photons of $\sim$1. The precise temperatures depend on the model details, in particular the presence of PAHs, the grain size, the gas/dust ratio, and the presence of excess UV over that of the stellar photosphere (Jonkheid et al. 2004, 2006, 2007; Kamp & Dullemond 2004; Nomura & Millar 2005; Nomura et al. 2007). For interstellar-sized grains ($\sim$0.1 μm), the models readily give surface temperatures of 100 K or more out to at least 100 AU. Even models in which the dust grains have grown and settled to the midplane have warm surface layers as long as some PAHs are still present. The total mass contained in this warm layer, however, is small, $\sim$1% or less of the total disk mass. For the specific 0.07 $M_\odot$ disk studied by Jonkheid et al. (2004) the mass at $T > 100$ K is $\sim$0.7 M_J. Thus, for a typical disk mass of 0.01 $M_\odot$, this may be as low as 0.1 M_J, below our upper limits.

The H_2 line fluxes from a protoplanetary disk representative of that around TW Hya have been modeled by Nomura & Millar (2005). These models include not just thermal excitation but also UV pumping of the H_2 levels. Nomura et al. (2007) include X-ray irradiation and the effect of grain size distributions. For the higher excitation lines the grain size distribution is particularly important with a distribution toward smaller grain sizes producing higher line strengths. This result is consistent with that

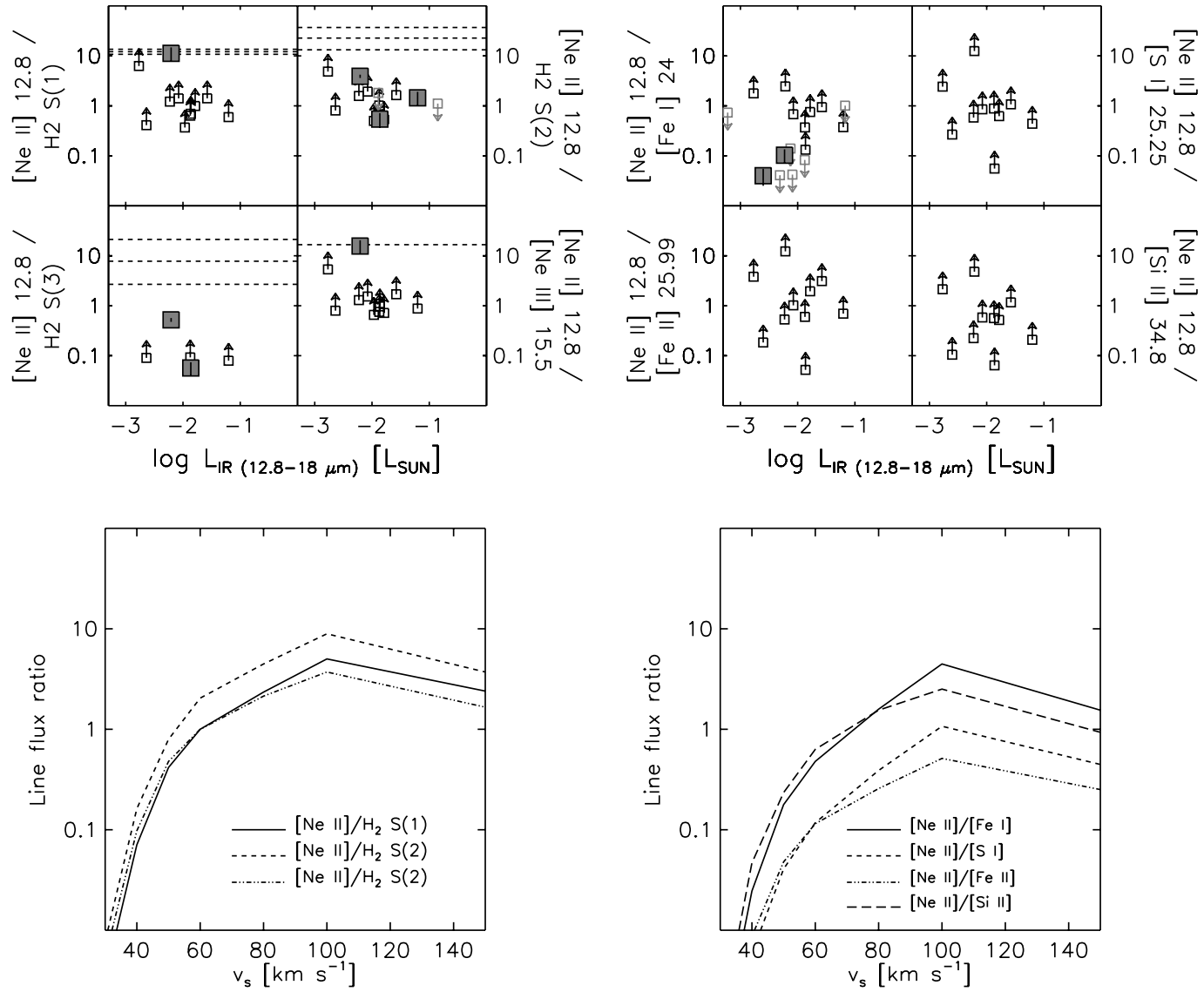

FIG. 10.—Line ratios of [Ne II] with respect to other species as functions of mid-IR luminosity. Large filled squares are used for sources with both [Ne II] and the second line detected. Small open squares with arrows indicate lower and upper limits of the line ratios. The dashed lines in the top left plot show the line ratios for the predictions from the Glassgold et al. (2007) and Nomura et al. (2007) models. The bottom two plots show the ratios from shock models by Hollenbach & McKee (1989) for different shock velocities.

of Jonkheid et al. (2007), who find lower temperatures in models with grain growth. Figure 7 shows the distribution of the observed line strengths with the predicted line strengths for the Nomura et al. (2007) model included for grain size distributions with maximum grain sizes of $a_{\max} = 10$ μm, 1 mm, and 10 cm. It is seen that the observed upper limits are all consistent with this model, even if excess UV is included. Note, however, that pure rotational H_2 line fluxes are extremely sensitive to the model details: small changes in the heating and cooling processes, as well as the treatment of the H/H_2 transition zone, can result in significant differences in gas temperatures and an order-of-magnitude variation in predicted line fluxes (see discussion in Li et al. 2002; Roellig et al. 2007). Therefore, comparison of the total mass of warm gas between models and observations is equally relevant.

Toward six sources (~8% of the sample), H_2 0–0 $S(2)$ and/or $S(3)$ emission is observed, which provides evidence for the presence of a significant hot ($T \gtrsim 500$ K) gas component in the disks. Hot gas ($T \gtrsim 500$ K) is observed toward a number of sources through the H_2 0–0 $S(2)$ line, most convincingly toward Sz 102, EC 82, Ced 110 IRS 6, EC 74, and EC 92. For Sz 102 a number of higher transition lines are also seen. The observed H_2 0–0 $S(2)$ line strengths are more than a factor of 10 higher than those predicted in Nomura & Millar (2005) and Nomura et al. (2007; see Fig. 7). Given the nondetection of the $S(1)$ line toward the same sources, which is predicted to have a similar strength, this is an indication that these disks have an additional source of emission from hot molecular hydrogen. The upper limits for H_2 0–0 $S(2)$ and $S(3)$ are higher for almost all sources than the Nomura & Millar (2005) predicted values. An additional hot component may therefore be present in these sources as well below our detection limit.

None of the sources with evidence for an additional hot component show evidence for PAH emission (see Geers et al. 2006). Of the eight sources with detected H_2 0–0 $S(2)$, four show strong [Ne II] emission, giving support to the idea of a common heating

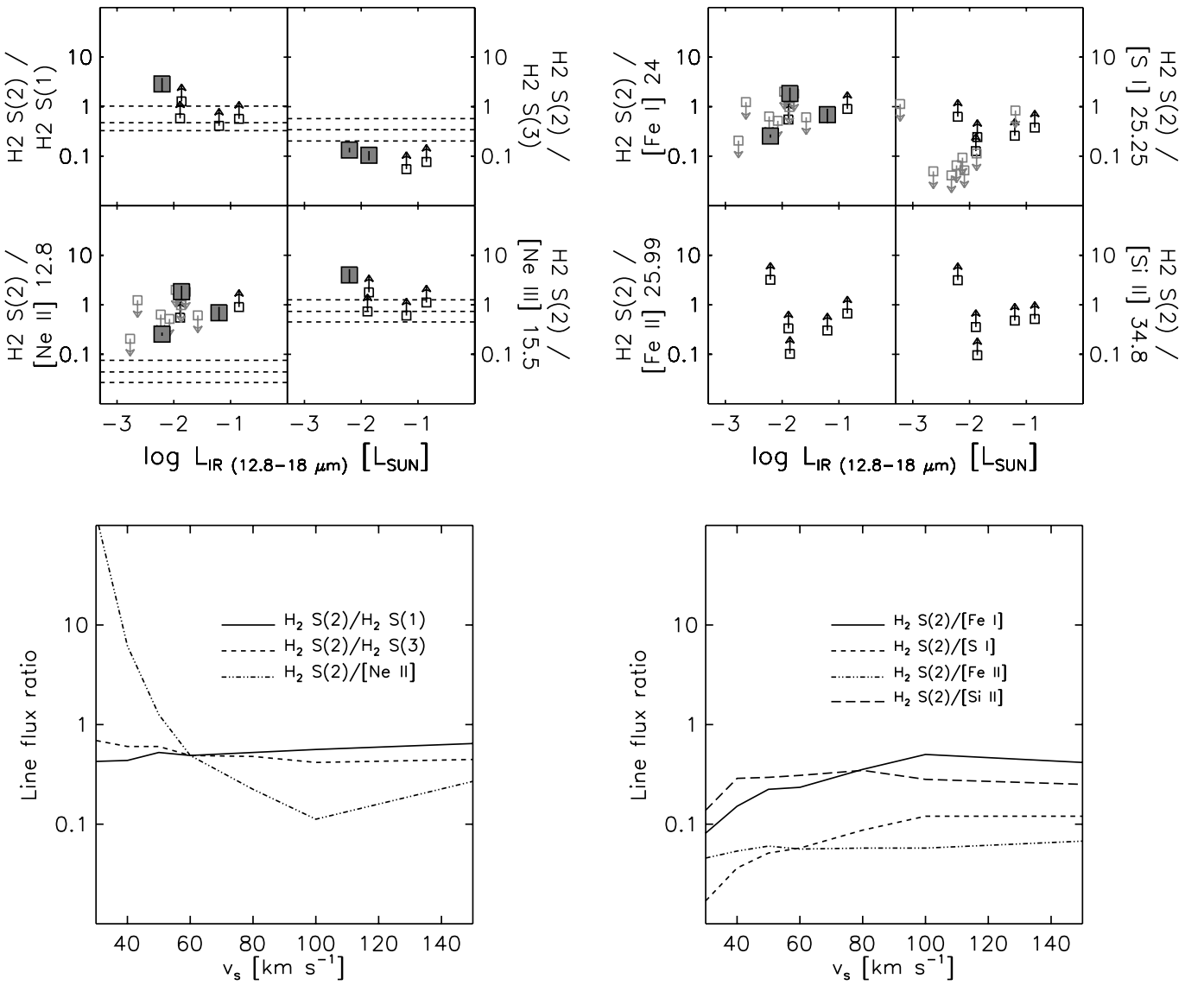

FIG. 11.—Same as Fig. 10, but for H_2 $S(2)$.

and excitation mechanism through X-rays or EUV. Of the [Ne II] sources two, T Cha and RR Tau, show strong PAH emission. Considering the limitations in observing the PAH emission as described by Geers et al. (2006) we can at this stage draw no conclusions about the relation between the hot H_2 emission, [Ne II] emission, and the importance of PAHs and small grains.

An origin in a high-velocity shock as discussed in § 5.1.3 could produce the enhanced $S(2)$ and $S(3)$ line strengths while keeping the line strengths of $S(0)$ and $S(1)$ reduced. However, as discussed in § 5.1.3, the main problem with invoking shocks to explain [Ne II] and H_2 is to accommodate both the detections of [Fe I] and the nondetections of [S I] and [Fe II] 26 μm. Figure 11 shows the observed and model line ratios with respect to H_2, similar to those in Figure 10. An origin in an oblique stellar wind shock faces the same problems as discussed for [Ne II] in § 5.1.3.

6. CONCLUSIONS

A survey of the mid-infrared gas phase pure rotational lines of molecular hydrogen and a number of atomic fine-structure transitions has been carried out toward a significant sample of 76 circumstellar disks with the *Spitzer* IRS. The principal findings include the following.

1. [Ne II] is detected toward ~20% of the sources and [Ne III] tentatively in one source. The [Ne II] detections and the [Ne II]/[Ne III] line flux ratio are consistent with disk heating and excitation of [Ne II] through X-rays as presented in Glassgold et al. (2007). Excitation through EUV radiation may contribute. Better constraints on the X-ray luminosities and [Ne III] fluxes are required to distinguish the two contributions.

2. [Fe I] is detected toward ~9% of the sources. No other low-excitation atomic lines, such as [Fe II], [S I], and [Si II], are detected. This suggests that these sources may possess optically thick disks with gas masses of at least 0.1 M_J.

3. Except for a tentative detection toward Sz 102, no compact H_2 0–0 $S(0)$ and $S(1)$ emission is observed toward any of the sources in our sample, setting limits of a few Jovian masses on the mass of the warm $T_{ex} = 100$ K gas in the disks. These limits are above model predictions. The H_2 line flux upper limits are also consistent with recent T Tauri disk model predictions by, for

example, Nomura et al. (2007). Earlier tentative *ISO* detections of H_2 in two Herbig Ae disks are not confirmed.

4. Hot ($T \gtrsim 500$ K) H_2 gas has been detected toward $\sim$8% of the sources. Given the high upper limits for the rest of the sources, the fraction may be higher. The detection of the hot gas suggests the presence of an additional source of hot H_2 emission not included in the most recent disk models (e.g., Nomura et al. 2007).

5. An origin of the enhanced H_2 emission in oblique shocks due to winds interacting with the disk surface is not consistent with the nondetection of atomic lines, in particular the nondetections of [S I] and [Fe II] 26 μm.

The bright [Ne II] lines detected at 12.8 μm are excellent targets for follow-up observations with high-dispersion echelle spectrometers on 8–10 m class telescopes (such as TEXES and VISIR). The measured spatial profiles and line shapes would provide exacting tests of the X-ray mediated disk emission proposed here and could definitely rule out any high-velocity shock mechanism.

The authors would like to thank Jes Jørgensen for making the *Spitzer* IRAC mosaics and Hideko Nomura for communicating her latest disk model results. Astrochemistry in Leiden is supported by a NWO Spinoza grant and a NOVA grant. Support for this work, part of the *Spitzer* Legacy Science Program, was provided by NASA through contracts 1224608, 1230779, and 1256316 issued by the Jet Propulsion Laboratory, California Institute of Technology, under NASA contract 1407. We thank the Lorentz Center in Leiden for hosting several meetings that contributed to this paper.

REFERENCES

Alcala, J. M., Krautter, J., Covino, E., Neuhaeuser, R., Schmitt, J. H. M. M., & Wichmann, R. 1997, A&A, 319, 184
Alexander, R. D., Clarke, C. J., & Pringle, J. E. 2005, MNRAS, 358, 283
———. 2006, MNRAS, 369, 216
Allers, K. N., Kessler-Silacci, J. E., Cieza, L. A., & Jaffe, D. T. 2006, ApJ, 644, 364
Andre, P., & Montmerle, T. 1994, ApJ, 420, 837
Appenzeller, I., Krautter, J., & Jankovics, I. 1983, A&AS, 53, 291
Audard, M., Briggs, K., Grosso, N., Guedel, M., Scelsi, L., Bouvier, J., & Telleschi, A. 2007, A&A, 468, 379
Baraffe, I., & Chabrier, G. 1996, in ASP Conf. Ser. 98, From Stars to Galaxies, ed. C. Leitherer, U. Fritze-von-Alvensleben, & J. Huchra (San Francisco: ASP), 209
Barsony, M., Kenyon, S. J., Lada, E. A., & Teuben, P. J. 1997, ApJS, 112, 109
Bary, J. S., Weintraub, D. A., & Kastner, J. H. 2003, ApJ, 586, 1136
Beckwith, S. V. W., Sargent, A. I., Chini, R. S., & Guesten, R. 1990, AJ, 99, 924
Beichman, C. A., Neugebauer, G., Habing, H. J., Clegg, P. E., & Chester, T. J. 1988, *Infrared Astronomical Satellite* (*IRAS*) Catalogs and Atlases, Vol. 1: Explanatory Suppl. (Pasadena: JPL)
Beichman, C. A., et al. 1984, ApJ, 278, L45
Blake, G. A., & Boogert, A. C. A. 2004, ApJ, 606, L73
Bouwman, J., de Koter, A., Dominik, C., & Waters, L. B. F. M. 2003, A&A, 401, 577
Brittain, S. D., Rettig, T. W., Simon, T., Kulesa, C., DiSanti, M. A., & Dello Russo, N. 2003, ApJ, 588, 535
Brown, J. M., et al. 2007, ApJ, in press
Calvet, N., D'Alessio, P., Hartmann, L., Wilner, D., Walsh, A., & Sitko, M. 2002, ApJ, 568, 1008
Cambresy, L., Copet, E., Epchtein, N., de Batz, B., Borsenberger, J., Fouque, P., Kimeswenger, S., & Tiphene, D. 1998, A&A, 338, 977
Carballo, R., Wesselius, P. R., & Whittet, D. C. B. 1992, A&A, 262, 106
Carkner, L., Kozak, J. A., & Feigelson, E. D. 1998, AJ, 116, 1933
Carr, J. S., Tokunaga, A. T., & Najita, J. 2004, ApJ, 603, 213
Casali, M. M., & Eiroa, C. 1996, A&A, 306, 427
Churchwell, E., & Koornneef, J. 1986, ApJ, 300, 729
Cieza, L. A., et al. 2007, ApJ, in press (astro-ph/0706.0563)
Clark, F. O. 1991, ApJS, 75, 611
Clarke, C. J., Gendrin, A., & Sotomayor, M. 2001, MNRAS, 328, 485
Cunha, K., Hubeny, I., & Lanz, T. 2006, ApJ, 647, L143
D'Alessio, P., Calvet, N., Hartmann, L., Franco-Hernández, R., & Servín, H. 2006, ApJ, 638, 314
D'Alessio, P., Calvet, N., Hartmann, L., Lizano, S., & Cantó, J. 1999, ApJ, 527, 893
Dartois, E., Dutrey, A., & Guilloteau, S. 2003, A&A, 399, 773
Decin, L., Morris, P. W., Appleton, P. N., Charmandaris, V., Armus, L., & Houck, J. R. 2004, ApJS, 154, 408
de Geus, E. J., de Zeeuw, P. T., & Lub, J. 1989, A&A, 216, 44
Dent, W. R. F., Greaves, J. S., & Coulson, I. M. 2005, MNRAS, 359, 663
de Zeeuw, P. T., Hoogerwerf, R., de Bruijne, J. H. J., Brown, A. G. A., & Blaauw, A. 1999, AJ, 117, 354
Drake, J. J., Testa, P., & Hartmann, L. 2005, ApJ, 627, L149
Dullemond, C. P., & Dominik, C. 2004, A&A, 417, 159
Dullemond, C. P., Hollenbach, D., Kamp, I., & D'Alessio, P. 2007, in Protostars and Planets V, ed. B. Reipurth, D. Jewitt, & K. Keil (Tucson: Univ. Arizona Press), 555
Dutrey, A., Guilloteau, S., & Simon, M. 2003, A&A, 402, 1003
Duvert, G., Guilloteau, S., Ménard, F., Simon, M., & Dutrey, A. 2000, A&A, 355, 165
Edwards, S., Fischer, W., Hillenbrand, L., & Kwan, J. 2006, ApJ, 646, 319
Elias, J. H. 1978, ApJ, 224, 453
Enoch, M. L., et al. 2006, ApJ, 638, 293
Evans, N. J., II, et al. 2003, PASP, 115, 965
Feigelson, E. D., & Lawson, W. A. 2004, ApJ, 614, 267
Forrest, W. J., et al. 2004, ApJS, 154, 443
Gauvin, L. S., & Strom, K. M. 1992, ApJ, 385, 217
Geers, V. C., et al. 2006, A&A, 459, 545
Glassgold, A. E., Najita, J. R., & Igea, J. 2007, ApJ, 656, 515
Gondoin, P. 2006, A&A, 454, 595
Gorti, U., & Hollenbach, D. 2004, ApJ, 613, 424
Gray, R. O., & Corbally, C. J. 1994, AJ, 107, 742
Greene, T. P., Wilking, B. A., Andre, P., Young, E. T., & Lada, C. J. 1994, ApJ, 434, 614
Habart, E., Natta, A., Testi, L., & Carbillet, M. 2006, A&A, 449, 1067
Haisch, K. E., Jr., Barsony, M., Greene, T. P., & Ressler, M. E. 2002, AJ, 124, 2841
Haisch, K. E., Jr., Lada, E. A., & Lada, C. J. 2001, ApJ, 553, L153
Hartigan, P. 1993, AJ, 105, 1511
Hartmann, L., Megeath, S. T., Allen, L., Luhman, K., Calvet, N., D'Alessio, P., Franco-Hernandez, R., & Fazio, G. 2005, ApJ, 629, 881
Hartmann, L., & Raymond, J. C. 1989, ApJ, 337, 903
Harvey, P. M., et al. 2006, ApJ, 644, 307
Herbig, G. H., & Bell, K. R. 1988, Lick Obs. Bull., Catalog of Emission Line Stars of the Orion Population 3 (Santa Cruz: Lick Obs.)
Hollenbach, D., & McKee, C. F. 1989, ApJ, 342, 306
Hollenbach, D. J., Yorke, H. W., & Johnstone, D. 2000, in Protostars and Planets IV, ed. V. Mannings, A. P. Boss, & S. S. Russell (Tucson: Univ. Arizona Press), 401
Hollenbach, D., et al. 2005, ApJ, 631, 1180
Houck, J. R., et al. 2004, ApJS, 154, 18
Hughes, J., Hartigan, P., Krautter, J., & Kelemen, J. 1994, AJ, 108, 1071
Hurt, R. L., & Barsony, M. 1996, ApJ, 460, L45
Ichikawa, T., & Nishida, M. 1989, AJ, 97, 1074
Jensen, E. L. N., & Mathieu, R. D. 1997, AJ, 114, 301
Jonkheid, B., Dullemond, C. P., Hogerheijde, M. R., & van Dishoeck, E. F. 2007, A&A, 463, 203
Jonkheid, B., Faas, F. G. A., van Zadelhoff, G.-J., & van Dishoeck, E. F. 2004, A&A, 428, 511
Jonkheid, B., Kamp, I., Augereau, J.-C., & van Dishoeck, E. F. 2006, A&A, 453, 163
Kaas, A. A. 1999, AJ, 118, 558
Kamp, I., & Dullemond, C. P. 2004, ApJ, 615, 991
Kenyon, S. J., Brown, D. I., Tout, C. A., & Berlind, P. 1998, AJ, 115, 2491
Kenyon, S. J., Dobrzycka, D., & Hartmann, L. 1994, AJ, 108, 1872
Kenyon, S. J., & Hartmann, L. 1995, ApJS, 101, 117
Kessler-Silacci, J., et al. 2006, ApJ, 639, 275
Koerner, D. W., & Sargent, A. I. 1995, AJ, 109, 2138
Lada, C. J., & Wilking, B. A. 1984, ApJ, 287, 610
Ladd, E. F., Lada, E. A., & Myers, P. C. 1993, ApJ, 410, 168
Lahuis, F., & Boogert, A. 2003, in SFChem 2002, Chemistry as a Diagnostic of Star Formation, ed. C. L. Curry & M. Fich (Waterloo: NRC Press), 335

Lahuis, F., et al. 2006a, ApJ, 636, L145
———. 2006b, c2d Spectroscopy Explanatory Suppl. (Pasadena: *Spitzer* Science Center)
Lawson, W. A., Feigelson, E. D., & Huenemoerder, D. P. 1996, MNRAS, 280, 1071
Li, W., Evans, N. J., II, Jaffe, D. T., van Dishoeck, E. F., & Thi, W.-F. 2002, ApJ, 568, 242
Lopez, C. E., & Girard, T. M. 1990, PASP, 102, 1018
McMullin, J. P., Mundy, L. G., Blake, G. A., Wilking, B. A., Mangum, J. G., & Latter, W. B. 2000, ApJ, 536, 845
Meyer, M. R., Wilking, B. A., & Zinnecker, H. 1993, AJ, 105, 619
Meyer, M. R., et al. 2006, PASP, 118, 1690
Myers, P. C., Fuller, G. A., Mathieu, R. D., Beichman, C. A., Benson, P. J., Schild, R. E., & Emerson, J. P. 1987, ApJ, 319, 340
Najita, J., Carr, J. S., & Mathieu, R. D. 2003, ApJ, 589, 931
Nomura, H., Aikawa, Y., Tsujimoto, M., Nakagawa, Y., & Millar, T. J. 2007, ApJ, 661, 334
Nomura, H., & Millar, T. J. 2005, A&A, 438, 923
Parenago, P. P. 1954, Tr. Gos. Astron. Sternberga, 25, 1
Parker, N. D. 1991, MNRAS, 251, 63
Pascucci, I., et al. 2006, ApJ, 651, 1177
———. 2007, ApJ, 663, 383
Persi, P., et al. 2000, A&A, 357, 219
Piétu, V., Dutrey, A., & Guilloteau, S. 2007, A&A, 467, 163
Pollanen, M. D., & Feldman, P. A. 1995, PASP, 107, 617
Pontoppidan, K. M., & Dullemond, C. P. 2005, A&A, 435, 595
Pontoppidan, K. M., Dullemond, C. P., van Dishoeck, E. F., Blake, G. A., Boogert, A. C. A., Evans, N. J., II, Kessler-Silacci, J. E., & Lahuis, F. 2005, ApJ, 622, 463
Pontoppidan, K. M., Stapelfeldt, K. R., Blake, G. A., van Dishoeck, E. F., & Dullemond, C. P. 2007, ApJ, 658, L111
Preibisch, T. 2003, A&A, 410, 951
Preibisch, T., et al. 2005, ApJS, 160, 401
Qi, C., Wilner, D. J., Calvet, N., Bourke, T. L., Blake, G. A., Hogerheijde, M. R., Ho, P. T. P., & Bergin, E. 2006, ApJ, 636, L157
Reipurth, B., Nyman, L.-A., & Chini, R. 1996, A&A, 314, 258
Richter, M. J., Jaffe, D. T., Blake, G. A., & Lacy, J. H. 2002, ApJ, 572, L161
Roellig, M., et al. 2007, A&A, 467, 187
Rydgren, A. E. 1980, AJ, 85, 444
Sako, S., Yamashita, T., Kataza, H., Miyata, T., Okamoto, Y. K., Honda, M., Fujiyoshi, T., & Onaka, T. 2005, ApJ, 620, 347
Sargent, B., et al. 2006, ApJ, 645, 395
Schegerer, A., Wolf, S., Voshchinnikov, N. V., Przygodda, F., & Kessler-Silacci, J. E. 2006, A&A, 456, 535
Sheret, I., Ramsay Howat, S. K., & Dent, W. R. F. 2003, MNRAS, 343, L65
Stelzer, B., Micela, G., & Neuhäuser, R. 2004, A&A, 423, 1029
Sternberg, A., & Neufeld, D. A. 1999, ApJ, 516, 371
Straizys, V., Cernis, K., & Bartasiute, S. 1996, Baltic Astron., 5, 125
Takeuchi, T., Clarke, C. J., & Lin, D. N. C. 2005, ApJ, 627, 286
Telleschi, A., Guedel, M., Briggs, K. R., Audard, M., & Palla, F. 2007, A&A, 468, 425
Thi, W. F., et al. 2001, ApJ, 561, 1074
van Boekel, R., Min, M., Waters, L. B. F. M., de Koter, A., Dominik, C., van den Ancker, M. E., & Bouwman, J. 2005, A&A, 437, 189
van Boekel, R., Waters, L. B. F. M., Dominik, C., Bouwman, J., de Koter, A., Dullemond, C. P., & Paresce, F. 2003, A&A, 400, L21
van den Ancker, M. E., de Winter, D., & Tjin A Djie, H. R. E. 1998, A&A, 330, 145
van Zadelhoff, G.-J., van Dishoeck, E. F., Thi, W.-F., & Blake, G. A. 2001, A&A, 377, 566
Ward-Thompson, D. 1993, MNRAS, 265, 493
Werner, M. W., et al. 2004, ApJS, 154, 1
Whittet, D. C. B., Prusti, T., Franco, G. A. P., Gerakines, P. A., Kilkenny, D., Larson, K. A., & Wesselius, P. R. 1997, A&A, 327, 1194
Wilking, B. A., Lada, C. J., & Young, E. T. 1989, ApJ, 340, 823
Wolk, S. J., Harnden, F. R., Jr., Flaccomio, E., Micela, G., Favata, F., Shang, H., & Feigelson, E. D. 2005, ApJS, 160, 423
Zhang, C. Y., Laureijs, R. J., & Clark, F. O. 1988, A&A, 196, 236